Numerical modeling of crack formation in powder forming processes

J.A. Hernández [a,c,*], J. Oliver [b], J.C. Cante [c], R. Weyler [c]

[a] International Center for Numerical Methods in Engineering (CIMNE), Technical University of Catalonia, Edificio C1, Campus Norte, Jordi Girona 1-3, Barcelona 08034, Spain
[b] E.T.S. d'Enginyers de Camins, Canals i Ports, Technical University of Catalonia, Edificio C1, Campus Norte, Jordi Girona 1-3, Barcelona 08034, Spain
[c] E.T.S. d'Enginyeries Industrial i Aeronàutica de Terrassa, Technical University of Catalonia, C/Colom, 11, Terrassa 08222, Spain

ARTICLE INFO

ABSTRACT

This paper presents a constitutive model describing the mechanical behavior of metal powders during (uniaxial) cold die compaction processes, placing special emphasis on the modeling of cracks formed during the ejection stage. The constitutive relationships are derived within the general framework of rate-independent, isotropic, finite strain elastoplasticity. The yield condition is determined by three surfaces intersecting non-smoothly in stress space, namely, an elliptical cap and the classical Von Mises and Drucker–Prager yield surfaces. The distinct irreversible processes are described in terms of two internal variables: an internal hardening variable, associated with accumulated compressive (plastic) strains, and an internal softening variable, linked with accumulated (plastic) shear strains. Motivated by both numerical and physical reasons, a *parabolic plastic potential function* is introduced to characterize the plastic flow on the linear Drucker–Prager failure surface. A thermodynamically consistent calibration procedure is employed to relate the softening modulus to fracture energy values obtained experimentally on Distaloy AE powder specimens. The predictive capability of the constitutive model is checked by simulating three representative cases: a diametral compression test, the ejection of an over-densified thin cylindrical part and the compaction of an axially symmetric multilevel part in an advanced CNC press machine. These simulations demonstrate the ability of the model to *detect evidence of macroscopic cracks*, *clarify and provide reasons* for the formation of such cracks, and evaluate, at least *qualitatively*, the influence of variations in the input variables on their propagation through the green compact.

© 2010 Elsevier Ltd. All rights reserved.

1. Introduction

Powder metallurgy (P/M) is a manufacturing technology in which net or near-net parts are produced from metallic powders. In its more usual sequence, the powders are first compressed (compaction) into a discrete shape and then heated (sintering) to cause bonding of the powder particles into a rigid mass. In this work, we are concerned exclusively with the finite element (FE) analysis of the former operation in its most classical form: (uniaxial) cold die compaction.

To date, the vast majority of FE modeling efforts in the P/M community has been directed towards understanding the densification process that takes place during the pressing stage; for recent reviews, see Brewin et al. (2007). As a result, considerable progress has been made in the prediction of final density distributions and punch forces. Despite this progress, however, the existing modeling tools have not matured to a point of enjoying widespread use in P/M design offices, and P/M products are still designed and

developed, almost exclusively, on the basis of practical rules and trial-and-error experience. According to Brewin and Federzoni (2006), one of the main barriers that hinders industrial exploitation of FE modeling technology is the inability of the existing simulation softwares to predict the *formation of cracks* during compaction. Cracks in P/M *green* compacts is one the major quality problems experienced by the P/M industry; perhaps the foremost in the case of ferrous components.

It is precisely the goal of this paper to attempt to satisfy this demand of the P/M industry by developing a constitutive model that describes, in an *unified* manner, both the consolidation mechanism and the potential formation of cracks in P/M compaction processes. The problem is certainly a very complex one: to the obvious difficulty of characterizing, from a continuum point of view, a material that evolves from an initial powdered state to a brittle solid form, one is faced with the elusiveness of modeling an inherently discontinuous phenomenon as cracking.[1] Furthermore, these phenomena (hardening and cracking) are intimately

---

* Corresponding author at: International Center for Numerical Methods in Engineering (CIMNE), Technical University of Catalonia, Edificio C1, Campus Norte, Jordi Girona 1-3, Barcelona 08034, Spain. Tel.: +34 699109594.
E-mail address: jhortega@cimne.upc.edu (J.A. Hernández).

[1] Not to mention the *contact* response between the pressing tools and the powder, that is to be meticulously computed so that no "spurious cracks" are induced. For details on the employed contact algorithm, the reader is referred to the author's works: Oliver et al. (2009), Hartmann et al. (2009), Hartmann et al. (2010).

interconnected, for the brittleness of the green compact depends on the level of densification.

Previous works by Cante (1995), Oliver et al. (1996), Weyler (2000) constitute the basis of the proposed model concerning the description of the consolidation mechanism (hardening). In order to originate our considerations from the most general standpoint possible, and, in turn, ensure satisfaction of the second law of thermodynamics, the isotropic plasticity Drucker–Prager/Cap type model elaborated in these works is reformulated and embedded in a thermodynamic framework. New ingredients are also incorporated: an apparently novel "parabolic" plastic potential function for the Drucker–Prager envelope, that attempts to alleviate the numerical shortcomings associated to purely isochoric flow rules; a density-dependent Von Mises yield surface, to improve the fit to experimental yield stress data at high densities; and a *softening* law, to account for the decrease in strength associated with cracking. The calibration of this softening law – in terms of *fracture energy* data obtained experimentally by Jonsén et al. (2007) – is another contribution of this work.

Cracks are modeled as localized high gradients of inelastic strains, which are induced – the gradients – by the abovementioned strain softening. To alleviate the acclaimed shortcoming of lack of convergence upon refinement of the finite element mesh, a regularization technique based on a characteristic length that depends on the spatial discretization has been used (Oliver, 1989). However, no ingredient to avoid mesh-induced directional bias has been included; finite element with embedded discontinuity (see e.g. Mosler and Meschke, 2004) and other sophisticated methods for realistically capturing crack discontinuities have not been contemplated either. From a rigorous Fracture Mechanics point of view, this aspect of the model can be certainly subject to criticism. However, these criticisms are somewhat blunted if we consider that the rationale behind the need for crack modeling in P/M compaction is rather distinct that in those problems that falls within the realm of classical Fracture Mechanics. Indeed, the ultimate goal of Fracture Mechanics is to determine how the structural strength of a structural or mechanical component is affected by cracks (as a function of their *size*) and to estimate its safe operational life (Broek, 1988). P/M cold compaction, by contrast, is an *intermediate* manufacturing operation – the compact is seldom commercialized in its unsintered state; if, upon visual inspection, a macroscopic crack is detected in a green compact, the exact dimensions of such a crack, or its influence on the mechanical performance of the finished part, are irrelevant for practical purposes: the part will be rejected anyway. The real concern of P/M practitioners when a crack is detected is to clarify its root cause so that corrective and preventive measures – be it the modification of the sequence of tooling motions or the replacement of a damaged punch – can be taken. The goal of numerical simulations is thus to merely provide insight and guide engineering judgement in such inquiries. The model should be able to capture evidence of macroscopic cracking but *without the necessity of giving an accurate and detailed description of the growth conditions*; undue sophistication is not warranted. A reasonable similarity between the crack (diffuse) pattern predicted by the model and that observed experimentally would suffice to consider the prediction as successful.

As mentioned above, the majority of continuum models proposed in the field of P/M compaction has been devoted to characterize the consolidation mechanism. The route to identify cracks in these models is normally by scrutinizing density distributions so as to find "suspiciously" intense gradients that may indicate the presence of shear cracks (Federzoni et al., 1999; Chtourou et al., 2002a). However, a substantial part of the cracks detected in green compacts is generated during the pressure release and ejection stages (Zenger and Cai, 1997). Density distributions remain practically unchanged during these process steps and, therefore, examination

of density fields can hardly reveal these post-pressing defects. Attempts to specifically model cracking in P/M compaction have been made by Coube and Riedel (2000), Lewis and Khoei (2001), Tahir and Ariffin (2006), Jonsén and Häggblad (2007)). In Tahir's work, a stress-based fracture criterion in conjunction with an advanced remeshing technique are employed to track meticulously the propagation of a *single* crack during the pressing of a flanged component. The model by Jonsén and Häggblad (2007) incorporates a *fictitious* crack with an appropriate cohesive law to study fracture process in a diametral compression test. The approach in these contributions are quite similar to that in genuine Fracture Mechanics problems: the existence of a crack is presumed and emphasis is placed on the accurate reproduction of its propagation throughtout the compact. According to the argument set forth previously, such models, at present, can hardly provide answers to practical questions in P/M processes. The approach adopted by Coube and Riedel (2000) and Lewis and Khoei (2001), by contrast, is more close to our point of view. Coube and Riedel (2000) consider the possibility of softening by making the cohesive strength and cohesion slope of a Drucker–Prager yield criterion state dependent variables; Lewis and Khoei (2001) study the prediction of localization phenomenon at the final stage of compaction by using an isochoric (Von Mises) yield criterion equipped with a softening law. However, none of these works deals with the characteristic length concept above mentioned. Furthermore, in Coube and Riedel (2000) the evolution equations of the variables governing the failure surface are derived without acknowledging the fracture energy of the material, and in Lewis and Khoei (2001), the employed Von Mises yield criterion predicts a totally unrealistic and unacceptable symmetry in the compressive-tensile behavior of the material under consideration.

The paper is organized as follows: Section 2 is devoted to the derivation of the constitutive equations that describe the powder behavior; the consistency of the proposed constitutive model with the second law of thermodynamics is discussed in Appendix A. In Section 3, the time integration of the constitutive laws and other mathematical aspects related with the solution algorithm are addressed in an abridged manner. Finally, Section 4 is concerned with the assessment of the formulation and numerical implementation of the model.

2. Constitutive model

2.1. Kinematics of plastic large deformations

Consider the powder as a deformable body $\mathcal{B}$ consisting of continuously distributed material occupying, at a reference time t_0, a region Ω_0 of $\mathbb{R}^n (n = 2, 3)$. The deformation at time t relative to the reference configuration is given by a one-to-one $\mathcal{C}^2$ mapping $\boldsymbol{\varphi} : \Omega_0 \to \Omega_t \subset \mathbb{R}^n$. As is customary in the literature of powder compaction modeling (Brown and Weber, 1988; Oliver et al., 1996; Bier and Hartmann, 2006; Rossi et al., 2007), we adopt the assumption of the local multiplicative decomposition of the deformation gradient of $\boldsymbol{\varphi}$, denoted by $\mathbf{F}$, into plastic and elastic parts:

$$\mathbf{F} = \widehat{\mathbf{F}}_e \cdot \mathbf{F}_p, \tag{1}$$

where $\mathbf{F}_p$ represents a pure plastic deformation from Ω_0 to a certain stress-free *intermediate configuration* (Simo and Hughes, 1998), and $\widehat{\mathbf{F}}_e$ a pure elastic loading from such a intermediate configuration to the current configuration Ω_t. For the particular case of die compaction modeling of standard metallic powders, which is the one that concerns us, it is also usual to assume (Cante, 1995; Oliver et al., 1996; Weyler, 2000) that elastic deformations are comparatively small. We shall thus limit our considerations to a kinematic description that considers *arbitrarily large plastic deformations* and small *elastic strains*. Under such circumstances, the distinction between

the abovementioned intermediate state and the current configuration Ω_t becomes negligible, and tensorial fields defined naturally at the intermediate configuration can be transformed directly into spatial tensorial fields. A valuable implication of this is that the Almansi strain tensor $\mathbf{e}(\mathbf{x}) = 1/2(\mathbf{1} - \mathbf{F}^{-T} \cdot \mathbf{F}^{-1})$ inherits the *additive* structure of classical small strain formulations (Khan and Huang, 1995):

$$\mathbf{e} = \mathbf{e}_e + \mathbf{e}_p, \tag{2}$$

being $\mathbf{e}_p = 1/2(\mathbf{1} - \mathbf{F}_p^{-T} \cdot \mathbf{F}_p^{-1})$ and $\mathbf{e}_e$ the plastic and elastic parts, respectively, of the Almansi strain tensor. This property, that, incidentally, holds also for the rate of deformation tensor:

$$\mathbf{d} = \mathbf{d}_e + \mathbf{d}_p, \tag{3}$$

will afford a remarkable aspect of simplicity in deriving the ensuing constitutive equations.

2.2. Thermodynamic framework

With a view towards deriving the constitutive laws on the basis of sufficient conditions to satisfy the thermodynamic requirement of positive dissipation, we begin the formulation of the proposed constitutive model by postulating the existence of a Helmholtz free energy function ψ, defined per unit reference volume. Since thermal effects are ignored (only *cold compaction* is considered here), the current value of this free energy function ψ at a point $\mathbf{X}$ will depend only on the history of deformation at its neighborhood. In this respect, we adopt the hypothesis, advocated by Mandel and others (Lubliner, 1990), according to which the free energy depends on the current value of the deformation gradient $\mathbf{F}$ only through its elastic part $\mathbf{e}_e$[2]:

$$\psi = \psi(\mathbf{e}_e, \boldsymbol{\xi}). \tag{4}$$

The other argument $\boldsymbol{\xi}$ represents collectively the set of scalar, strain-like *internal variables* Since the evolution of these variables are related with irreversible mechanisms, it seems reasonable to classify $\boldsymbol{\xi}$ according to the nature of the internal physical changes associated with each mechanism. Specifically, we categorize the set of internal variables into internal *hardening* variables, ξ^h, and internal *softening* variables, ξ^s. Thus, $\partial\psi/\partial\xi^h \cdot \dot\xi^h \geqslant 0$ would represent the rate at which mechanical energy, per unit reference volume, is stored due to interlocking of rough grains, plastic deformation, cold welding of particles and other microscopic events macroscopically correlated with a *strain-hardening tendency*. By contrast, $\partial\psi/\partial\xi^s \cdot \dot\xi^s \leqslant 0$ would account for the release of energy associated with the breakage of interparticle bonds, i.e. *cracking*, due to combinations of tensile and shear straining. Such microstructural alterations become manifest on the macroscopic scale as material *softening*.

As for the set of internal hardening variables ξ^h, a review of the literature on powder compaction modeling shows that the proposal of using a single internal hardening variable in terms of the accumulated compressive plastic strain (Chtourou et al., 2002b; Tszeng and Wu, 1996; Erhart et al., 2005; Cante, 1995) prevails over other more complex theories that also acknowledge that plastic flow may be activated by distorsional deformation in the later stages of compaction (Cocks and Sinka, 2006). In this study, we simply adopt the former classical approach. In particular, the internal hardening variable at time t, henceforth denoted by ξ^h, is defined as

$$\xi^h(t) = \xi^{h0} e^{-\int_{t_0}^{t} \mathrm{tr}\mathbf{d}_p dt}, \quad \text{with} \quad \mathrm{tr}\ \mathbf{d}_p(t) < 0, \tag{5}$$

---

[2] The smallness of the elastic strains permits to write directly – i.e., without violating any invariance requirement, ψ in terms of $\mathbf{e}_e$.

or in rate form:

$$\dot\xi^h = -\xi^h \mathrm{tr}\ \mathbf{d}_p \quad \text{with} \quad \mathrm{tr}\ \mathbf{d}_p(t) < 0, \tag{6}$$

where tr$\mathbf{d}_p$ stands for the trace of the plastic part of the rate of deformation tensor. The reason for this particular choice for the expression of ξ^h comes from the fact that, defined in this way, ξ^h can be practically identified with the relative density $\eta = \rho/\rho\mathrm{th}$($\rho\mathrm{th}$ is the *theoretical* density of the metal or alloy concerned), thereby being very easy to monitor and record experimentally. The similarity becomes readily apparent by comparing Eq. (6) with the rate, dimensionless form of the conservation of mass $\dot\eta = -\eta\mathrm{tr}\ \mathbf{d}$ (recall that elastic strains are assumed to be negligible and hence $\mathbf{d}_p \approx \mathbf{d}$).

While the selection of appropriate internal hardening variables has long been the subject of debate in the powder compaction modeling community (see Cocks and Sinka, 2006), references to the use of internal softening variables are practically non-existing in the related literature, at least within a formal thermodynamic framework. In this work, assumptions made in this regard will be thereby based on physically plausible considerations, borrowed mainly from constitutive theories of other cohesive-frictional materials, rather that on experimental evidences. Firstly, we shall presume that the amount of softening depends only on the length of the trajectory in the plastic strain space (*strain softening* hypothesis). Since cracks in PM parts are provoked mainly by combination of tensile and shear forces, it is reasonable to define, as commonly done in granular material modeling contexts (Regueiro and Borja, 1999), the softening state variables in terms of dilatational and shear, accumulated inelastic strains, i.e.:

$$\xi_1^s = \int_{t_0}^{t} \|dev\ \mathbf{d}_p\| dt, \quad \text{with} \quad \mathrm{tr}\ \mathbf{d}_p(t) > 0, \tag{7}$$

$$\xi_2^s = \int_{t_0}^{t} \mathrm{tr}\ \mathbf{d}_p\ dt, \quad \text{with} \quad \mathrm{tr}\ \mathbf{d}_p(t) > 0. \tag{8}$$

A complete discussion of the relative influence on the material response of the above defined shear and dilatant internal softening variables, ξ_1^s and ξ_2^s, respectively, requires some notions on the employed yield condition and flow rules, and therefore, it is deferred to later sections.

For purposes of deriving the elastic constitutive law, it proves convenient to introduce the following additive decomposition for the free energy function:

$$\psi\left(\mathbf{e}_e, \xi^h, \boldsymbol{\xi}^s\right) = \psi_e\left(\mathbf{e}_e, \xi^h\right) + \psi_p\left(\xi^h, \boldsymbol{\xi}^s\right), \tag{9}$$

where ψ_e and ψ_p stand for the elastic and plastic parts, respectively. Note that, as distinct from the standard uncoupled decomposition used in metal plasticity theory (Simo, 1999, 1998), and also invoked by some authors in the specific field of powder compaction modeling (see Oliver et al., 1996; Weyler, 2000; Bier and Hartmann, 2006; Mähler and Runesson, 2003), the elastic part ψ_e does depend on the internal hardening variable. This in accord with the experimentally observed fact that elastic properties of metallic powders exhibit a marked dependency on volumetric strains (Riera, 1999; Pavier and Dorémus, 1996). In the following, we address this issue, and an expression for ψ_e is provided. In regard to the plastic counterpart ψ_p, on the contrary, we are compelled by mathematical difficulties to adopt a more pragmatic approach. No explicit functional form for ψ_p will be furnished, and hardening/softening laws will be hence derived without invoking any thermodynamic potential. In Appendix A, however, it is rigorously demonstrated that this shift towards pragmatism does not induce any thermodynamic inconsistency, and the constitutive model, consequently, does fulfil the requirement of positive dissipation.

2.3. Elastic response

Motivated by the smallness of the elastic strains, the structure of the elastic free energy function is assumed to be quadratic in the elastic strains:

$$\psi_e \left(\mathbf{e}_e, \xi^h \right) = \frac{1}{2} \mathbf{e}_e : \mathbf{c}_e \left(\xi^h \right) : \mathbf{e}_e, \tag{10}$$

where $\mathbf{c}_e$ denotes the fourth-order elasticity tensor in the current configuration. By virtue of the Coleman–Noll procedure (Lubliner, 1990), we arrive at the following stress–elastic strains constitutive law:

$$\boldsymbol{\tau}(\mathbf{x}) = \frac{\partial \psi}{\partial \mathbf{e}_e} = \mathbf{c}_e : \mathbf{e}_e, \tag{11}$$

where $\boldsymbol{\tau}$ denotes the Kirchhoff stress tensor. Furthermore, although it is recognized that anisotropic effects influence the elastic response, specially at high densities (see Coube and Riedel, 2000), a precise knowledge of how to characterize the material anisotropy induced during densification is still lacking. As a result, anisotropy effects are commonly neglected in modeling powder compaction (Brekelmans et al., 1991; Oliver et al., 1996; Brown and Weber, 1988; Bier and Hartmann, 2006). In the present work, this simplifying assumption is also adopted; the expression for $\mathbf{c}_e$ reduces hence to:

$$\mathbf{c}_e = \kappa^e \left(\xi^h \right) \mathbf{1} \otimes \mathbf{1} + 2\mu^e \left(\xi^h \right) \left(\mathbf{I}_{\mathbf{sym}} - \frac{1}{3} \mathbf{1} \otimes \mathbf{1} \right), \tag{12}$$

wherein $\mathbf{1}$ denotes the second-order identity tensor and $\mathbf{I}_{\mathbf{sym}}$ symbolizes the symmetric fourth-order identity tensor. Note that expression (12) is practically identical to its counterpart in classical infinitesimal theory. The only difference is that the bulk modulus κ^e and shear modulus μ^e are not constant but dependent on the hardening internal variable; i.e.:

$$\kappa^e = \frac{E^e \left(\xi^h \right)}{3 \left(1 - 2 v^e \left(\xi^h \right) \right)} \quad \text{and} \quad \mu^e = \frac{E^e \left(\xi^h \right)}{2 \left(1 + v^e \left(\xi^h \right) \right)}, \tag{13}$$

where E^e and v^e denotes the Young's modulus and the Poisson's ratio, respectively. Such a dependence on ξ^h of the elastic parameters reflects the abovementioned coupling between elastic and strain hardening responses.

According to experiments conducted by Pavier (1998) on Distaloy AE powders, the Poisson's coefficient can be regarded, as a first approximation, as constant and equal to the value of the corresponding fully dense material ($v^e = 0.29$ for a Distaloy AE alloy). By contrast, E^e is strongly influenced by the level of densification attained in the pressing stage; however, there is no wide consensus on how it actually depends on ξ^h. The following exponential law corresponds to the fitting equation to Young's modulus values obtained in *triaxial test* carried out by Pavier (1998):

$$E^e \left(\xi^h \right) = \frac{\eta_0}{\xi^h} E_0 e^{B_E(\xi^h - \eta_0)}, \tag{14}$$

with E_0 = 1360.92 MPa and B_E = 8.82 for a Distaloy AE powder.[3] On the other hand, by using a rather distinct experimental procedure (velocity sound tests), Coube (1998) arrived at the following linear estimation:

$$E^e \left(\xi^h \right) = \frac{\eta_0}{\xi^h} \left(Y_{E1} + Y_{E2} \xi^h \right), \tag{15}$$

where Y_{E1} = −16383.47 MPa and Y_{E2} = 39073.95 MPa. The notorious discrepancy between these correlations suggests that the

commonly accepted, and also adopted in this work, hypothesis of linear elasticity (at constant density) might be questionable on fundamental grounds, and it may prove more appropriate to reconcile the discrepancy by using a non-linear elasticity law, as the one proposed by Mosbah (1995). The detailed discussion of such matters, however, goes beyond the scope of this work, and we shall simply attempt to alleviate the inconsistency by employing selectively expressions (14) and (15). Specifically, in view of the experimental procedures from which these are drawn, it seems more reasonable to employ Pavier's empirical law (14) in describing the elastic behavior in *situations of confinement*, whereas, in circumstances closer to unstressed configurations, Coube's relation (Eq. (15)) appears more adequate.

2.4. Yield condition

The yield condition used in this work is derived, essentially, from the Drucker–Prager type "cap" criterion proposed by Oliver et al. (1996). This yield condition is formulated in terms of the Kirchhoff stress invariants[4] $p = \frac{1}{3} I_1 = \frac{1}{3} \mathrm{tr}\, \boldsymbol{\tau}$ (mean stress), and $q = \sqrt{2J_2} = \sqrt{dev\, \boldsymbol{\tau} : dev\, \boldsymbol{\tau}}$, and it is determined by two yield surfaces, namely, an *elliptical* cap centered at the origin, whose equation reads:

$$\phi^e = q^2 + s_2^2 p^2 - s_1^2 s_2^2 = 0, \tag{16}$$

and a classical Drucker–Prager envelope, which is a straight line in the p–q plane:

$$\phi^d = q + \alpha p - c = 0. \tag{17}$$

The parameters s_1 in Eq. (16) is the major axis of the ellipse (see Fig. 1(a)) and it corresponds to the *hydrostatic yield stress in compression*. The eccentricity of the ellipse s_2 is related to the radial to axial stress ratio k_{tr}, also known as the *pressure transmission coefficient* (Doremus et al., 2001; Cunningham, 2005), through the following expression:

$$s_2 = \sqrt{\frac{3(1 - k_{\mathrm{tr}})}{1 + 2k_{\mathrm{tr}}}}, \tag{18}$$

as it can be inferred by analyzing the stress state, ignoring elastic effects, in a hydrostatic compression test (Hernández, 2009). Variable c in Eq. (17) is customarily referred to as *cohesion*, and it can be interpreted as the shear strength under zero hydrostatic stress (intersection of the Drucker–Prager yield surface with the q-axis); α represents the slope of the Drucker–Prager line and is termed the *parameter of internal friction*.

These four constitutive parameters (s_1, s_2, c and α) are regarded as state functions, that is, they depend, in principle, on both the internal hardening variable ξ^h and the set of internal softening variables ξ^s. The so-called hardening laws relate to the functional dependence of these parameters on the internal hardening variable; hereafter, we shall attach a subscript "h" to the corresponding variable symbol to refer to its hardening counterpart, e.g. $c_{\mathrm{h}} = c(\xi^h)|_{\xi^s=0}$.

Hardening laws are adjusted empirically[5] from yield stress data obtained at different densities and along different loading paths. For the major axis of the elliptical cap s_1, we shall employ the empirical

---

[3] Note that the elastic free energy function (10) was defined per unit reference volume, hence the necessity of the (approximated) Jacobian factor η_0/ξ^h.

[4] We should remark that, in casting the yield condition in terms of stress invariants, we are tacitly making the debatable assumption (see Storåkers et al., 1999) that anisotropic effects are negligible.

[5] In fact, we should point out that the proposed form for the yield condition in stress space (elliptical cap + Drucker–Prager yield surface) has been deduced from stress-density data obtained from compaction tests, i.e., involving solely strain hardening behavior. Thus, the tacitly assumed fact that the yield locus maintains this shape also during process entailing strain softening is, although physically plausible, an experimentally unconfirmed one.
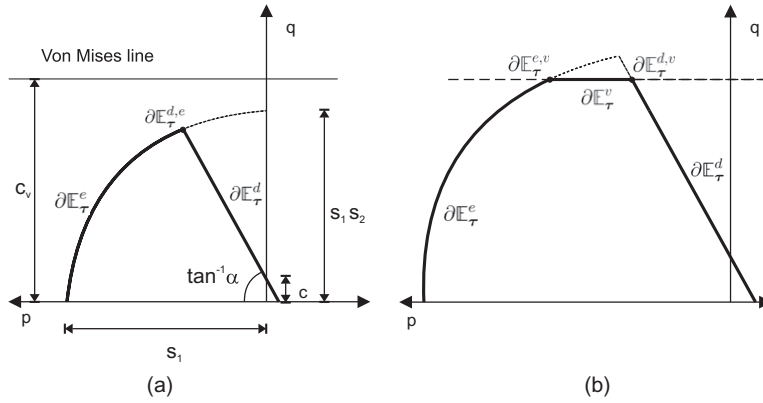
Fig. 1. Yield surfaces for two different states: (a) Drucker–Prager + elliptical cap, for moderate level of compaction (b) Drucker–Prager + elliptical cap + Von Mises, for high level of compaction (close to full density).
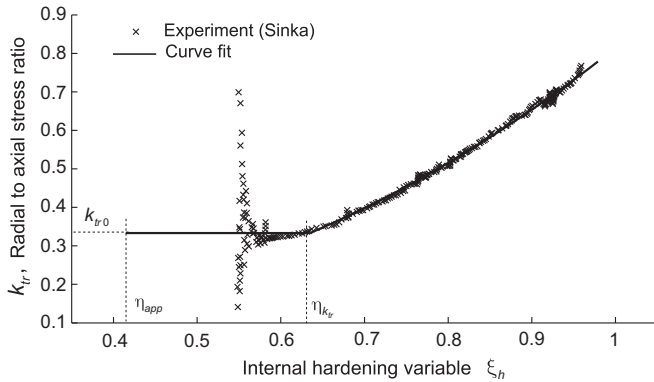

Fig. 2. Radial to axial stress ratio versus internal hardening variable ξ^h. Experimental data obtained from simulated closed die compactions conducted by Sinka and Cocks (2007) on Distaloy AE powder specimens.

correlation obtained by Pavier (1998) from triaxial tests on Distaloy AE powder specimens:

$$s_{1h}(\xi^h) = \frac{\eta_0}{\xi^h} A_{s_1} \left(\ln \left(\frac{1 - \eta_{app}}{1 - \xi^h} \right) \right)^{\frac{1}{N_{s_1}}}, \tag{19}$$

where[6] η_{app} denotes the relative apparent density. The fitted constant for a Distaloy AE alloy with $\rho_0 = \rho_{app} = 3.04$ g/cm^3 and ρth = 7.33 g/cm^3 are $A_{s_1} = 95.4439$ MPa and $N_{s_1} = 0.6506$. As for the eccentricity, in Fig. 2 we show radial to axial stress ratio measures, collected by Sinka and Cocks (2007) on Distaloy AE powder specimens for several relative (inelastic) densities. Observe that experimental information is only available for $\xi^h > 0.55$ and, additionally, data points in the range 0.55–0.635 are widely scattered – a fact attributable to the lack of accuracy in monitoring stress values at this density range on powder materials. To resolve this uncertainty in experimental information at low densities, we resort to predictions of micromechanical models for the early stages of compaction; these predictions estimate that the initial radial to axial stress ratio is $k_{tr0} = 1/3$ (Cocks and Sinka, 2006). Accordingly, we propose an empirical correlation in which the pressure transmission coefficient is set to a constant value k_{tr0} for low values of ξ^h:

$$k_{tr}(\xi^h) = \begin{cases} k_{tr0}, & \text{if } \xi^h \leqslant \eta_{k_{tr}}, \\ (\xi^h - \eta_{k_{tr}})(A_{k_{tr}} \xi^h + B_{k_{tr}}) + k_{tr0}, & \text{if } \xi^h > \eta_{k_{tr}}. \end{cases} \tag{20}$$

---

[6] Recall that the factor η_0/ξ^h appears to put into correspondence *true* stress data with Kirchhoff stress values.

where $A_{k_{tr}} = 1.074$, $B_{k_{tr}} = 0.242$, $k_{tr0} = 1/3$ and $\eta_{k_{tr}} = 0.635$. The hardening law $s_{2h} = s_{2h}(\xi^h)$ is obtained simply by substituting the above expression into Eq. (18).

By performing various sets of fracture tests on Distaloy AE powder specimen, Coube (1998) determined the location in the p–q stress space of the Drucker–Prager yield surface as a function of the compaction density, and arrived at the following exponential relationship for the cohesion variable:

$$c_h(\xi^h) = \sqrt{\frac{2}{3}} \frac{\eta_0}{\xi^h} c_h^{cy} = \sqrt{\frac{2}{3}} \frac{\eta_0}{\xi^h} A_{c_h} e^{B_{c_h} \xi^h}. \tag{21}$$

with $A_{c_h} = 0.001$ MPa and $B_{c_h} = 11.2368$. From the same experimental study, it was concluded that the parameter of internal friction α may be regarded, approximately, as independent of ξ^h, hence $\alpha_h = \alpha_{h0} = 2.29$ (for Distaloy AE powders).

Experimental isodensity yield stress points in the p–q space – obtained by Pavier (1998) for Distaloy AE powders – are presented in Fig. 3.a; the sequence of yield surfaces constructed according to the proposed hardening laws (Eqs. (19), (18) and (21)) are also shown in this figure. While the adjustment can be considered satisfactory for moderate level of densification, at high densities it is clear that the yield condition determined by the Drucker–Prager line and the hardening cap over-predicts the yield stress of the material in the vicinity of their intersection, to such an extent that the physically unattainable threshold σ_y – the yield strength of the fully dense material – is exceeded at a relative density $\eta \approx \xi^h = 0.982$. To improve this deficient adjustment in the range of high densities ($\eta > 0.92$), the yield condition is refined by incorporating a third yield surface: a pressure-independent Von Mises yield locus, represented graphically as an horizontal line in the p–q plane (see Fig. 1(b)), and whose equation reads:

$$\phi^v = q - c_v = 0. \tag{22}$$

The improvement derived from using a three-yield surfaces criterion can be readily appreciated by comparing Fig. 3(a) and (b). The values of the Von Mises constitutive parameter c_{vh} deduced from Fig. 3(b) are plotted, in turn, in Fig. 4(b) versus the hardening state variable ξ^h. The hardening law resulting from fitting these points is approximately quadratic in ξ^h and it is only defined for $\xi^h \geqslant 0.92$. In order to put the evolution of c_{vh} in a mathematically suitable form, we suppose that, for $\xi^h < 0.92$, the Von Mises yield surface is *reduced* to a point that coincides with the intersection between the other two yield surfaces (see Fig. 4(a)). The following analytical expression reflects this consideration:
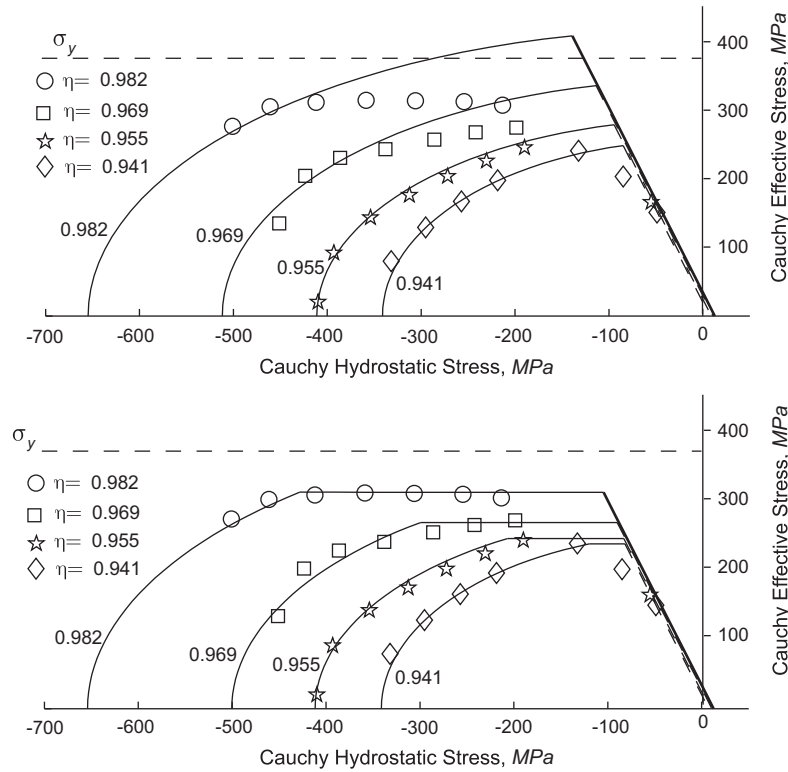
Fig. 3. Experimental yield stress data (as a function of relative density η) from consolidated and over-consolidated compression tests (Pavier, 1998) on Distaloy AE powder specimens. Isodensity contours employing: (a) Drucker–Prager + Elliptical cap, (b) Drucker–Prager + Elliptical cap + Von-Mises.
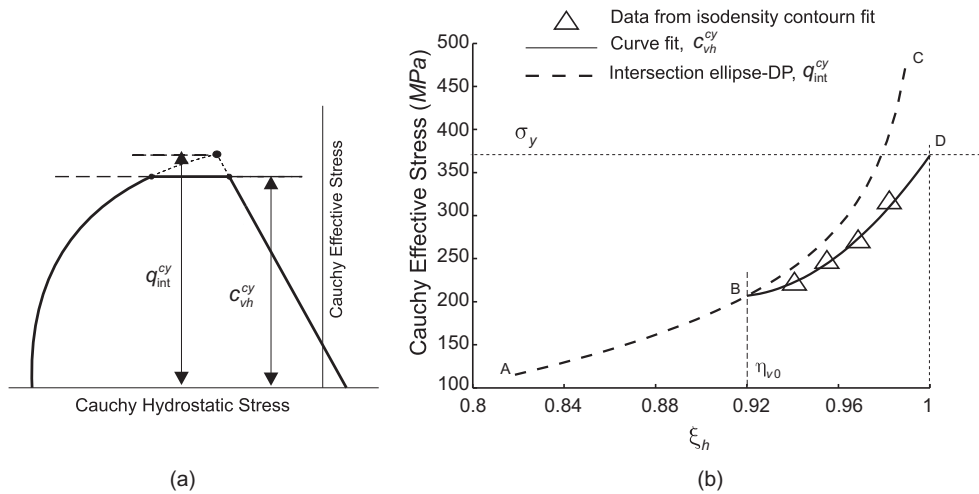
Fig. 4. (a) Definition of q_{int}^{cy} as the deviatoric stress measure at the intersection of the Drucker–Prager and the elliptical cap ($\partial\mathbb{E}_\tau^{d,e}$. (b) Von Mises parameter c_{vh} vs internal hardening variable ξ^h. The curve AC corresponds to $q_{int}^{cy} = q_{int}^{cy}(\xi^h)$, whereas BD is the quadratic fit to the data points obtained from the isodensity contours shown in 3(b).

$$c_{vh}\left(\xi^h\right) = \begin{cases} q_{int} = \sqrt{\tfrac{2}{3}}\tfrac{\eta_0}{\xi^h}q_{int}^{cy}, & \text{if } \xi^h \leqslant \xi_{v0}, \\ \sqrt{\tfrac{2}{3}}\tfrac{\eta_0}{\xi^h}\sigma_y\left(1 - A_{c_{vh}}\left(\xi^h - B_{c_{vh}}\right)(1 - \xi^h)\right), & \text{if } \xi^h > \xi_{v0}. \end{cases}$$

$$(23)$$

with[7] $A_{c_{vh}} = 58.160$, $B_{c_{vh}} = 0.8252$, σ_y = 370 MPa and $\xi_{v0} = 0.92$.

The use of a Von Mises yield criterion combined with an elliptical cap and a Drucker–Prager envelope can be found also in Coube and Riedel (2000). However, as distinct from our approach, in

which c_v is regarded as a state function, Coube considers a yield surface "fixed" in stress space, at a position determined by the yield strength of the fully dense material σ_y.

2.5. Flow rule

As is customary in the framework of incremental plasticity theory (Simo, 1999), we apply Koiter's generalization of the flow rule to obtain the plastic rate of deformation tensor $\mathbf{d}_p$ in terms of the plastic flow vectors $\mathbf{m}^\alpha$ associated to each yield surface:

$$\mathbf{d}_p = \sum_{\alpha \in \{e,d,v\}} \dot{\lambda}^\alpha \mathbf{m}^\alpha,$$

$$(24)$$

---

[7] The superscript "cy" indicates that the affected symbol is a Cauchy stress-like variable, as opposed to Kirchhoff stress-like variables.

the summation being over the number of yield surfaces.[8] The positive scalar factors $\dot{\lambda}^\alpha$, referred to as *consistency parameters* or *plastic multipliers* must obey the standard Karush–Kuhn–Tucker loading/unloading conditions, that in the context of *rate-independent* plasticity read:

$$\dot{\lambda}^\alpha \geqslant 0, \quad \phi^\alpha\left(\boldsymbol{\tau}, \xi^h, \xi^s\right) \leqslant 0, \tag{25}$$

and

$$\dot{\lambda}^\alpha \phi^\alpha\left(\boldsymbol{\tau}, \xi^h, \xi^s\right) = 0, \quad \text{(no sum on } \alpha\text{)}, \tag{26}$$

along with the consistency condition:

$$\dot{\lambda}^\alpha \dot{\phi}^\alpha\left(\boldsymbol{\tau}, \xi^h, \xi^s\right) = 0, \quad \text{(no sum on } \alpha\text{)}. \tag{27}$$

Furthermore, each plastic flow vector $\mathbf{m}^\alpha$ is presumed to be aligned with the gradient of a certain *plastic potential function* Q^α, i.e. $\mathbf{m}^\alpha = \partial Q^\alpha/\partial \boldsymbol{\tau}$. The assumption of *associative* flow rule on the elliptical yield surface has proved to be reasonably accurate for modeling most pressing processes (Cocks and Sinka, 2006). Accordingly, we shall presume that $\phi^e = Q^e$, i.e. the functional forms of the yield locus and the plastic potential function coincides; therefore, from Eq. (16), we get:

$$\mathbf{m}^e = \frac{\partial Q^e}{\partial \boldsymbol{\tau}} = 2 \, dev \, \boldsymbol{\tau} + \frac{2}{3} s_2^2 p \, \mathbf{1}. \tag{28}$$

Besides, by definition, the volumetric component of the plastic flow vector must be zero on the Von Mises yield surface. Therefore, the plastic flow vector $\mathbf{m}^v$ has only deviatoric contribution[9]:

$$\mathbf{m}^v = 2 \, dev \, \boldsymbol{\tau}. \tag{29}$$

2.5.1. Parabolic plastic potential function

Whereas the hypothesis of associated flow rule is generally accepted in the case of the elliptical cap, the direction of $\mathbf{d}_p$ when the stress point lies on the Drucker–Prager envelope is plagued by much controversy. Some authors simply extend the validity of the associative assumption and consider that $\mathbf{d}_p$ is normal to the failure line (Chtourou et al., 2002a; Erhart et al., 2005; Rossi et al., 2007). However, this hypothesis is clearly at odds with reality: it over-predicts the dilatational response of the material, as experimental studies carried out by Pavier (1998) and Sinka and Cocks (2007) evidence. These studies reveal that the direction of $\mathbf{d}_p$ is only adequately described by the normality condition in the elliptical cap portion. As the stress state approaches the interception with the Drucker–Prager yield surface, the plastic strain increment becomes steeper. Eventually, at the interception point $\partial \mathbb{E}_\tau^{e,d}$ (see Fig. 1(a)), $\mathbf{d}_p$ turns vertical and the nature of the plastic flow ceases to be compressive. Furthermore, according to Pavier (1998), $\mathbf{d}_p$ maintains this vertical orientation in the Drucker–Prager stress range covered by the experiments.

Motivated by these observations, some authors have favored the assumption of *isochoric* (or deviatoric) (tr $\mathbf{d}_p$ = 0) plastic flow on the Drucker–Prager yield surface (Weyler, 2000; Cante et al., 2005). However, the numerical integration of constitutive models with implicit backward Euler schemes (return mapping algorithms) is beset by some difficulties in the case of deviatoric flow rules. Roughly, the situation in which the so-called *elastic trial stress* happens to fall on the right-hand side of the Drucker–Prager apex is a singular one and requires, therefore, "special" algorithmic treatment. To clarify this issue, consider the two distinct trial states $\boldsymbol{\tau}_A^{tr}$ and $\boldsymbol{\tau}_B^{tr}$ plotted in Fig. 5. To calculate the projection onto the
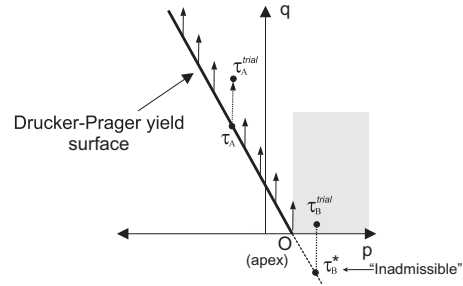

Fig. 5. Drucker–Prager yield surface with deviatoric plastic flow rule.

yield surface of a trial stress such as $\boldsymbol{\tau}_A^{tr}$, located on the left-hand side of the apex, we simply trace a vertical line – in virtue of the purely deviatoric nature of the plastic flow – passing through $\boldsymbol{\tau}_A^{tr}$ and, to ensure plastic consistency, obtain the intersection with the Drucker–Prager yield line. However, if the same procedure is indiscriminately applied to compute the updated stress corresponding to a trial state $\boldsymbol{\tau}_B^{tr}$ lying on the right-hand side of the apex (shaded region in Fig. 5), the outcome would be the inadmissible solution $\boldsymbol{\tau}_B^*$ – q is a norm and hence cannot be negative.

A review of the granular material modeling literature shows that the solutions put forward to alleviate this problem are, basically, of two types. On the one hand, one may introduce an additional cap to "round off" the linear potential function at that point (Duxbury and Li, 1996); on the other hand, one may resort to a different potential function meeting the requirement of smoothness at the apex (Etse and Willam, 1994; Kuhl et al., 2000; Vrech and Etse, 2006; Grassl and Jiràsek, 2006). Here the latter approach is adopted. The proposed *parabolic* plastic potential function, expressed as

$$Q^d\left(\boldsymbol{\tau}, \xi^h, \xi^s\right) = q^2 + \beta\left(\xi^h, \xi^s\right) p, \tag{30}$$

with $\beta > 0$, is adequate to this end, since the corresponding flow vector:

$$\mathbf{m}^d = \frac{\partial Q^d}{\partial \boldsymbol{\tau}} = 2 \, dev \, \boldsymbol{\tau} + \frac{1}{3} \beta \mathbf{1}, \tag{31}$$

is horizontal, in the p-q plane, at the apex (q = 0), and, consequently, the normals to the potential surface cover all possible return directions.

The equation Q^d = K, with K constant, defines a parabola in the p-q plane; hence the name of *parabolic* potential. The use of parabolic plastic potential functions can be traced back to Etse and Willam (1994), and it is frequently utilized for the characterization of failure mechanisms for cohesive frictional materials. However, there is a fundamental difference between these constitutive models and the one presented here. In Etse's model, both the yield and the potential functions are parabolic-shaped. The essence of our approach, by contrast, is to introduce a parabolic potential function, but maintaining[10] the classical (linear) Drucker–Prager yield criterion (see Fig. 6). In this way, the singularity at the vertex "O" is circumvented and, at the same time, the simplicity and the computational convenience of using a linear yield criterion is retained.

With such a proposal, one is faced with the task of determining a functional form for the state function $\beta = \beta(\xi^h, \xi^s)$. In order to avoid thermodynamically unreasonable results, the functional form of β must be consistent with the dissipation inequality

---

[8] e: elliptical cap; d: Drucker–Prager envelope; v: Von Mises yield surface.

[9] The factor two appears because we have chosen, to simplify the algebra, $Q^v(\boldsymbol{\tau}) = q^2$ as the plastic potential function associated to the Von Mises yield surface.

[10] Claims with regard to the necessity of "rounding off" the Drucker Prager yield surface at the apex for avoiding the singularity are unfounded, and might be ascribed to an over-exposure to associated plasticity.
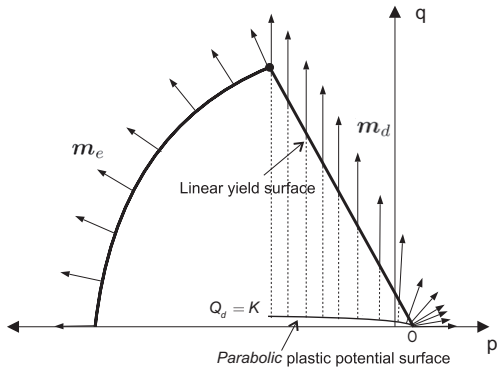
Fig. 6. Parabolic plastic potential surface, for γ close to zero.

$\mathcal{D} = \boldsymbol{\tau} : \mathbf{d} - \dot{\psi} = \boldsymbol{\tau} : \mathbf{d}_p - \dot{\psi}_p \geqslant 0$, which, for the case in which only the Drucker–Prager yield surface is active ($\dot{\xi}^h = 0$) reduces to:

$$\mathcal{D} = \boldsymbol{\tau} : \mathbf{d}_p - \frac{\partial \psi_p}{\partial \boldsymbol{\xi}^s} \cdot \dot{\boldsymbol{\xi}}^s \geqslant 0. \tag{32}$$

As outlined in Section 2.2, the term $\partial \psi_p / \partial \boldsymbol{\xi}^s \cdot \dot{\boldsymbol{\xi}}^s$ is associated with a release of energy, i.e. $\dot{\psi}_s \leqslant 0$. Hence, the worst conceivable circumstances for the satisfaction of inequality (32) correspond to the case $\dot{\boldsymbol{\xi}}^s = 0$. A sufficient condition for ensuring the positiveness of $\mathcal{D}$ is, therefore, that:

$$\boldsymbol{\tau} : \mathbf{d}_p \geqslant 0. \tag{33}$$

According to Eqs. (31) and (24), the plastic rate of deformation tensor takes the form:

$$\mathbf{d}_p = \dot{\lambda}^d \left(2 \, de\nu \, \boldsymbol{\tau} + \frac{1}{3} \beta \mathbf{1} \right), \quad \text{for } \boldsymbol{\tau} \in \partial \mathbb{E}_{\boldsymbol{\tau}}^d. \tag{34}$$

with $\dot{\lambda}^d \geqslant 0$. Substituting (34) into (33), and enforcing the yield condition (17), we arrive at:

$$\boldsymbol{\tau} : \mathbf{d}_p = \dot{\lambda}^d \left(2q^2 - \frac{\beta}{\alpha} q + \frac{\beta}{\alpha} c \right). \tag{35}$$

It is straightforward to show that the above inequality is fullfiled for all $q \geqslant 0$ provided that:

$$\left(\frac{\beta}{\alpha} \right)^2 - 8 \frac{c\beta}{\alpha} \leqslant 0 \Rightarrow \beta \leqslant 8c\alpha. \tag{36}$$

from which follows that a logical choice for the functional form of β is

$$\beta = \gamma c\alpha, \quad \text{with} \quad 0 \leqslant \gamma \leqslant 8. \tag{37}$$

The variable γ appearing in the above equation is intrinsically associated with the plastic *dilatancy* of the material. For values of γ close to zero, the plastic flow vector is practically isochoric in the whole range of stresses, as shown in Fig. 6, except in a small neighborhood at the apex, wherein the flow vector rotates until becoming purely dilatational at $q = 0$. It is apparent, thus, that for $\gamma \approx 0$, the proposed flow rule reproduces the experimental response observed by Pavier (1998).

2.6. Evolution equations for the internal variables

Having formulae (24), (28), (29) and (31) at hand, the evolution Eqs. (6)–(8) for the internal state variables ξ^h, ξ_1^s and ξ_2^s, respectively, can be recast in terms of the plastic multipliers and plastic flow vectors associated to each yield surface. Taking the trace of both sides of Eq. (24), it yields:

$$\text{tr}\mathbf{d}_p = \dot{\lambda}^e \text{tr}\mathbf{m}^e + \dot{\lambda}^d \text{tr}\mathbf{m}^d + \dot{\lambda}^\nu \text{tr}\mathbf{m}^\nu. \tag{38}$$

By straightforward operations on the experimentally calibrated parameters shown previously, it can be demonstrated that the elliptical cap lies entirely in the second quadrant of the p–q plane ($p < 0$) for any physically conceivable value of ξ^h. According to Eq. (28), this implies that tr $\mathbf{m}^e = 2s_2^2 p < 0$. Furthermore, from Eqs. (29) and (31), it follows that $\text{tr}\mathbf{m}^\nu = 0$ and $\text{tr}\mathbf{m}^d > 0$, respectively. These facts enable the rate form Eq. (6) for the internal hardening variable to be rephrased as

$$\dot{\xi}^h = -\xi^h \text{tr}\mathbf{d}_p = -\xi^h \dot{\lambda}^e 2s_2^2 p, \tag{39}$$

i.e., ξ^h *only evolves when the stress state lies on the elliptical cap* ($\dot{\lambda}^e > 0$). Similarly, since tr $\mathbf{m}^d > 0$ only when yielding occurs on the Drucker–Prager yield surface, the evolution Eqs. (7) and (8) for the internal softening variables can be rewritten as

$$\dot{\xi}_1^s = \|de\nu \, \mathbf{d}_p\| = 2\dot{\lambda}^d q, \tag{40}$$

and

$$\dot{\xi}_2^s = \text{tr}\mathbf{d}_p = \dot{\lambda}^d \gamma \alpha c; \tag{41}$$

From the above equations it follows that *stress states on the Drucker–Prager yield surface are unequivocally correlated with softening behavior*, i.e., cracking; hence the alternative denomination *failure surface* for the Drucker–Prager envelope.

2.6.1. Simplifications

One of the fundamental assumptions on which the proposed model built is that the magnitude of elastic strains is negligible in comparison with irrecoverable deformations.[11] This assumption allowed us to draw an approximation between ξ^h and the relative density η in loading processes with a steady accumulation of plastic deformation. By using Eq. (39), and exploiting the analogy with the conservation of mass equation, this approximation can be formally extended to cover any loading history:

$$\dot{\xi}^h = \xi^h \mathcal{H}(\dot{\eta}) \mathcal{H}(\dot{\lambda}^e) \frac{\dot{\eta}}{\eta} = \mathcal{H}(\dot{\lambda}^e \dot{\eta}) \frac{\dot{\eta}}{\eta}, \tag{42}$$

where $\mathcal{H}(\bullet)$ denotes the Heavyside step function. The factor $\mathcal{H}(\dot{\eta})$ in the above equation accounts for the fact that ξ^h can only evolve if $\dot{\eta} > 0$, i.e., if density increases at the analyzed point. The other Heaviside factor, $\mathcal{H}(\dot{\lambda}^e)$, adds the proviso that the elliptical yield surface must be active ($\dot{\lambda}^e > 0$) for ξ^h to increase. The major benefit arising from this approximation is that, once the sign of $\dot{\lambda}^e$ is known, the differential equation represented by expression (42) can be integrated in *closed-form*. It is important to emphasize that, as distinct to those approaches that assume directly that $\xi^h = \eta$, the internal variable defined through approximation Eq. (42) maintains the status of *non-decreasing, path-dependent* magnitude.

In accordance to Koiter's rule (24), when the updated stress lies on the intersection $\partial \mathbb{E}_{\boldsymbol{\tau}}^{d,e}$ between the Drucker–Prager failure surface and the elliptical cap, the consistency parameters $\dot{\lambda}^d$ and $\dot{\lambda}^e$ are nonzero and, therefore, the *hardening and softening mechanism act concurrently*; the strain hardening produced by densification is partially counterbalanced by the decrease in strength induced by strain softening. It is the authors' experience that this simultaneous occurrence of both hardening and softening can cause the return mapping algorithm to zigzag, placing in each iteration the solution on a different location without converging to any value. In the interest of computational robustness, thus, rate Eqs. (40)

---

[11] It can be shown that, in a monotonic (hydrostatic compressive) loading history the ratio between relative density and internal hardening variable is bounded by $|1 - e^{s_1/\kappa^e}|$. For the experimentally calibrated values shown previously, this factor is in the order 10^{-3}(see Hernández, 2009).
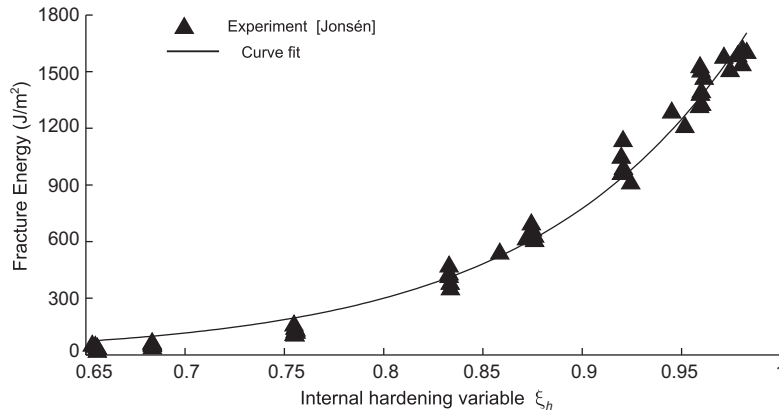
Fig. 7. Fracture Energy vs ξ^h. Experimental values provided by Jonsén et al. (2007) (Distaloy AE powder specimens), along with the exponential curve fit (see Eq. (45)).

and (41) are slightly altered to preclude this possibility; using the properties of the Heaviside step function $\mathcal{H}(\bullet)$, we can write:

$$\dot{\xi}_1^s = 2\left(1 - \mathcal{H}\left(\dot{\lambda}^e\right)\right)\dot{\lambda}^d q, \tag{43}$$

$$\dot{\xi}_2^s = \left(1 - \mathcal{H}\left(\dot{\lambda}^e\right)\right)\dot{\lambda}^d \gamma \alpha c. \tag{44}$$

This modification implies that, when the updated stress lies on the intersection point of the Drucker–Prager surface with the cap, only hardening takes place. Since there are no empirical laws accounting for the simultaneous occurrence of strain hardening and softening, this simplification does not actually compromise the correctness of neither the hardening laws shown previously nor the softening correlations that will be presented in the sequel.

2.7. Softening laws

To take developments a step forward, it is necessary to establish the functional relation between the state variables and the softening internal variables ξ^s, i.e., relations of the type $\dot{c}_s = \dot{c}(\xi^s)_{\xi^h=\text{const}}$.[12] However, experimental tests *directly* capturing how the yield strength at given point of the material diminishes with plastic deformation – at the same point – are not available: softening behavior – as opposed to the pointwise manifestation of hardening behavior – is characterized by inelastic deformation in localized regions accompanied by elastic unloading in the surrounding material (*strain localization*); thus, stress-displacement curves obtained from fracture tests cannot be converted *directly* into valid stress–strain relationships that reflects material properties. To calibrate the softening laws, thus, it is necessary to resort to an indirect method, amply employed in fracture modeling of granular materials, such as concrete (Oliver, 1989; Bicánic and Pearce, 1998; de Borst, 2001), that quantifies the deterioration of yield strength in terms of the *fracture energy* of the material, which is an experimentally obtainable quantity defined as the mechanical energy required for the formation of a unit of fracture surface. To the authors' knowledge, the unique experimental effort to date to determine the fracture energy of consolidated metallic powders has been made by Jonsén et al. (2007), who carried out diametral compression tests on Distaloy AE powder cylindrical specimens, previously compacted at various densities, to measure the energy spent in inducing fracture along the loaded diameter. The fracture energy values obtained in these tests are plotted in Fig. 7 against the (inelastic) relative density; an exponential equation seems to provide a good fit to these data:

$$\mathcal{G}_f^{(dct)}(\xi^h) = \frac{\eta_0}{\xi^h} A_{\mathcal{G}_f} e^{B_{\mathcal{G}_f}\xi^h}, \tag{45}$$

with $A_{\mathcal{G}_f} = 0.1487$ J/m^2 and $B_{\mathcal{G}_f} = 9.5102$.[13]

However, note that we have at our disposal only a set of fracture energy values, measured in a single test, while the number of softening laws to be calibrated amounts to five (one for each yield condition parameter). This relative paucity of experimental data to support such relations compels us to, based on practical considerations, introduce some simplifying assumptions. Green compacts are more prone to failure during pressure release and subsequent ejection stage. Upon pressure release, the stress state at every point of the compact moves away from the compressive stress region – close to the cap and the Von Mises yield surfaces – to the tensile/shear stress region, which, in turn, is bounded by the Drucker–Prager failure line. Therefore, the decay in compressive yield strength - determined by the elliptical cap and Von Mises yield surface parameters s_1, s_2 and c_v – during cracking processes seems of little concern from a practical point of view. Accordingly, we shall assume that *the shape and size of the elliptical cap and the Von Mises yield surface remain unaltered in the course of failure events*, and consequently, are completely determined by the current value of the internal hardening variable, i.e.:

$$\dot{s}_{1s} = 0 \rightarrow s_1\left(\xi^h, \xi^s\right) = s_1\left(\xi^h\right) = s_{1h}\left(\xi^h\right), \tag{46}$$

$$\dot{s}_{2s} = 0 \rightarrow s_2\left(\xi^h, \xi^s\right) = s_2\left(\xi^h\right) = s_{2h}\left(\xi^h\right). \tag{47}$$

$$\dot{c}_{vs} = 0 \rightarrow c_v\left(\xi^h, \xi^s\right) = c_v\left(\xi^h\right) = c_{vh}\left(\xi^h\right). \tag{48}$$

On the other hand, it can be easily shown that the uniaxial tensile strength is related to the Drucker–Prager parameters through the expression:

$$\sigma_t = \sqrt{\frac{3}{2}} \frac{\sqrt{6}c}{\sqrt{6}+\alpha}. \tag{49}$$

It follows from the above that a reduction in c is accompanied by a decrease in uniaxial tensile strength; and that variations of α also affects the rate at which σ_t diminishes. However, in the interest of simplicity, and since no experimental evidence confirms a distinct trend, we shall consider that cohesion and uniaxial tensile strength decrease at the same rate; or equivalently, that *the parameter of internal friction does not depend on ξ^s*, which, in accordance to the

---

[12] In keeping with notation convention introduced previously, a "*s*" subscript is appended to refer to the softening counterpart of each variable.

[13] It is important to remark that fracture energy values plotted in Fig. 7 are measures *per unit current surface*, which is the typical definition of fracture energy. However, in conformance with the rest of stress and energy quantities involved in the formulation of the constitutive equations, the fracture energy $\mathcal{G}_f^{(dct)}$ is defined on the reference configuration, i.e. it is an energy *per unit reference surface*, hence the factor $\frac{\eta_0}{\xi^h}$ in Eq. (45).

hypothesis put forward in Section 2.4, permits to regard α as a simple material constant:

$$\dot{\alpha}_s = 0 \rightarrow \alpha = \alpha_{h0}. \tag{50}$$

In view of the above simplifications, strain softening will be reflected in the p–q plane by a simple translation of the Drucker–Prager yield surface towards the origin. The task of establishing the set of softening laws is thus reduced to find the relationship $c_s = c_s(\xi^s)$. Motivated by the exponential structure of its hardening counterpart (Eq. (21)), the following correlation is proposed for this variable:

$$c_s(\xi_1^s, \xi_2^s) = c_0 \left(\exp \left(\frac{H_{01}\xi_1^s + H_{02}\xi_2^s}{c_0} \right) - 1 \right), \tag{51}$$

where H_{01} and H_{02} denote the *softening parameters* and c_0 stands for the cohesion at the moment t_{is} yielding on the Drucker–Prager yield surface commences, that is, $c_0 = c_h(\xi^h(t_{is}))$. Difficulties are encountered, again, in calibrating the softening law (51), since two constitutive parameters (H_{01} and H_{02}) have to be adjusted empirically and only one experiment is available. Thus, we have to whether neglect the influence of one of the internal variables, or to calibrate one of these parameters, say H_{01}, and consider the other one as a dependent variable $H_{02} = v_s H_{01}$, through a heuristically chosen factor v_s. The dilemma can be, apparently, resolved if we analyze the relative influence of both internal variables in the material response; dividing Eq. (44) by Eq. (43), we get:

$$\frac{\dot{\xi}s_2}{\dot{\xi}s_1} = \gamma \frac{\alpha c}{2q}. \tag{52}$$

It was set forth in Section 2.5 that, to reproduce the behavior observed experimentally, the dilatancy parameter γ should be set to values close to zero; it follows from Eq. (52), hence, that *the effect of shear plastic strain* dominates the material response ($\dot{\xi}_1^s \gg \dot{\xi}_2^s$), and therefore, *the influence of the volumetric internal variable can be disregarded* ($\dot{\xi}_2^s = 0$). Nevertheless, one has to be aware of the limitations imposed by this hypothesis. Its validity hinges on assuming that q is greater, or of the same order, as c (see Eq. (52)); this condition, although seldom, may fail in some circumstances. For instance, in an hypothetical hydrostatic *tensile* test, in which the stress state is such that $q = 0$, variable $\dot{\xi}_1^s$ would not evolve, and hence, unrealistically, no failure would be predicted. A similar situation may be encountered when the current stress lies in the vicinity of the apex of the Drucker–Prager yield surface.

By virtue of this simplification, the set of internal softening variables can be reduced to a single scalar variable $\xi^s = \xi_1^s$, and the softening law (51) rephrased as

$$c_s(t) = c_0 \left(\exp \left(\frac{H_0 \xi^s}{c_0} \right) - 1 \right). \tag{53}$$

The tangential slope H of the curve described by Eq. (53), defined by the following rate equation:

$$\dot{c}_s = H\dot{\xi}^s, \tag{54}$$

is typically termed the *continuum softening modulus* (Oliver, 2000). By differentiation of Eq. (53), H can be alternatively expressed as

$$H = H_0 \frac{c_0 + c_s}{c_0} = H_0 \frac{c}{c_0}. \tag{55}$$

2.7.1. Calibration of the softening law

We are now in the position to establish the correspondence between the softening parameter $H_0(\xi^h)$ and the experimentally obtained fracture energy values, given in Eq. (45). To this end, consider the work g_f, per unit reference volume, consumed when cohesion decreases from c_0 to zero:
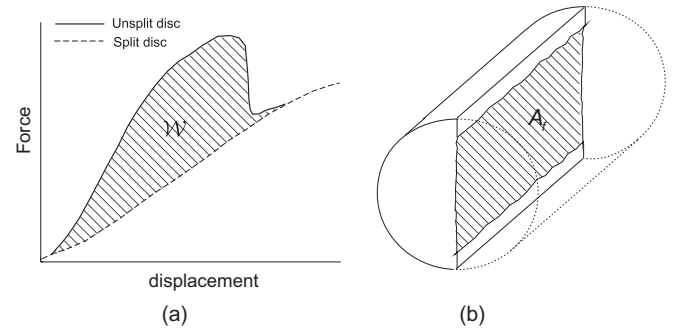
Fig. 8. (a) Typical force versus displacement graph for a diametral compression test. The solid curve corresponds to the monitored force until the fracture of the specimen. The dashed curve is the response of a specimen deliberately split into two halves (to measure the recoverable elastic energy). The energy $\mathcal{W}$ required to produce the crack is grossly estimated as the shaded area. (b) Area of the specimen employed to compute the fracture energy.

$$g_f = \int_{t_{is}}^{t_\infty} \boldsymbol{\tau} : \mathbf{d}_p \; dt. \tag{56}$$

Using the flow rule (34), the above equation can be rephrased as

$$g_f = \int_{t_{is}}^{t_\infty} \dot{\lambda}^d (2q^2 + \gamma\alpha cp) \; dt. \tag{57}$$

Employing Eqs. (43), (54) and (55), the plastic multiplier $\dot{\lambda}^d$ can be expressed in terms of the cohesion variable and the norm of deviatoric stress:

$$\dot{\lambda}^d = \frac{\dot{\xi}s}{2q} = \frac{c_0}{2H_0 cq} \dot{c}. \tag{58}$$

Substitution of Eq. (58) in Eq. (57) yields :

$$g_f = \int_{t_{is}}^{t_\infty} \frac{c_0}{2H_0 cq} (2q^2 + \gamma\alpha cp)\dot{c} \; dt = \frac{c_0}{2H_0} \int_{c_0}^{0} \frac{2q^2 + \gamma\alpha cp}{cq} \; dc. \tag{59}$$

The link between experimental data and the softening constitutive law is finally provided by the following balance of energy in the damaged volume Ω_f (Oliver, 1996):

$$\mathcal{W} = \mathcal{G}_f^{(dct)} A_f = \int_{\Omega_f} g_f(\mathbf{X}) dV. \tag{60}$$

where A_f denotes the area in which the crack *localizes* and $\mathcal{W}$ the total dissipated energy. The meaning of these terms is further clarified in Fig. 8.

Under the assumption, commonly adopted in the related literature (de Borst, 2001), that g_f is approximately uniform over Ω_f, and considering a localization bandwith l_f, the above expression takes the form:

$$\mathcal{G}_f^{(dct)} = g_f(\mathbf{X}) l_f. \tag{61}$$

Inserting Eq. (59) in Eq. (61), we finally get:

$$\mathcal{G}_f^{(dct)} = l_f \frac{c_0}{2H_0} \int_{c_0}^{0} \frac{2q^2 + \gamma\alpha cp}{cq} \; dc. \tag{62}$$

With a view towards minimizing the dependency to mesh refinement, the softening modulus is related to the localization bandwith[14] through the following expression:

$$H_0 = l_f \widehat{H}_0, \tag{63}$$

---

[14] The localization bandwith or *characteristic length* l_f is intimately tied to the size and orientation of the subsequent spatial discretization. See Oliver (1989) for further details.
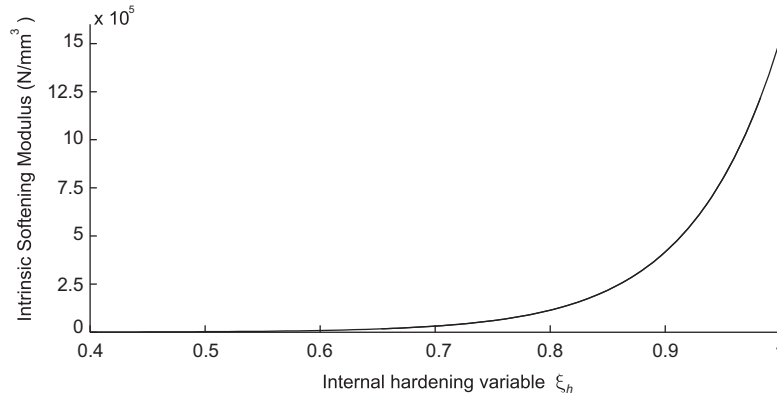
Fig. 9. Intrinsic softening parameter $\widehat{H}_0$ vs internal hardening variable ξ^h.

where $\widehat{H}_0$ stands for the so-called *intrinsic softening parameter* (Oliver, 2000), defined as

$$\widehat{H}_0 = \frac{c_0(\xi^h)}{2\mathcal{G}_f^{(dct)}} \int_{c_0}^{0} \frac{2q^2 + \gamma\alpha cp}{cq} \, dc. \tag{64}$$

A remark concerning notation is in order here. The superindex "*dct*" attached to the symbol $\mathcal{G}_f$ indicates that this quantity corresponds to the fracture energy measured in a diametral compression test; the intrinsic softening $\widehat{H}_0$, on the other hand, is not accompanied by any superindex. This notational convention has been deliberately introduced to highlight one of our basic assumptions in this regard: whereas *fracture energy is clearly a quantity sensitive to the loading history* followed during the experimental test, we shall consider that the intrinsic softening parameter does not depend on the loading history. In other words, *we regard the intrinsic softening parameter $\widehat{H}_0$ as a state function*, i.e., a quantity that can be uniquely determined at any time by the point values of the state variables. In this case, according to Eqs. (64) and (45), the softening parameter only depends on the internal hardening variable, that is $\widehat{H}_0 = \widehat{H}_0(\xi^h)$. The *intrinsic softening modulus* is, defined by analogy with Eq. (55) as

$$\widehat{H} = \widehat{H}_0 \frac{c_0 + c_s}{c_0}, \tag{65}$$

is thus also a state function, but it further depends on the internal softening variable, $\widehat{H} = \widehat{H}(\xi^h, \xi^s)$. Note that neither the softening modulus H nor the softening parameter H_0 can be viewed as state functions, since their value are affected by the spatial grid used in the computations.

To complete the calibration, it would be now pertinent to evaluate analytically the integral appearing in Eq. (64). To this end, one needs the analytical expression of the stress path traced during the de-cohesion process at points within the cracking band. For the case of a diametral compression test, the derivation of such expressions is far from being obvious, as may surmised from the stress analysis (in the elastic range) carried out by Timoshenko and Goodier (1970). To overcome this difficulty, it proves advantageous to exploit the fact that the diametral compression test is but an indirect test to measure the tensile strength of brittle or quasi-brittle materials (hence the alternative denomination of *indirect tension test* Wanga et al. (2003)), on which direct uniaxial tensile test are difficult to perform. The experimental configuration of the diametral compression test is such that the developing of the crack at the loaded diameter takes place under Mode I or opening mode conditions, which, in turn, are the same conditions encountered in a standard uniaxial tensile test. On this basis, a plausible assumption is to consider that the fracture energy measured in a

uniaxial tensile test is approximately equal to that corresponding to the diametral compression test, i.e.:

$$\mathcal{G}_f^{(dct)} \approx \mathcal{G}_f^{(tt)}, \tag{66}$$

the superindex "*tt*" signifying tensile test. Under such an assumption, the analytical evaluation of the integral in Eq. (64) becomes feasible, as we show in the following.

In a uniaxial tensile test, the ratio q/p at points belonging to the cracking band is approximately linear:

$$q \approx \hat{m} \, p, \tag{67}$$

since necking is not very pronounced in quasi-brittle materials (Hearn, 2000) and thus the uniaxial stress state prevails after bifurcation of the response. For a tensile test, $\hat{m} = \sqrt{6}$, as it can be easily deduced by simple algebra. Enforcing the yield condition in Eq. (67), we get an expression of q as a function of the cohesion variable c:

$$q = \frac{\hat{m}}{\hat{m} + \alpha} \, c = \tilde{m}c. \tag{68}$$

Inserting the above equation into Eq. (64) and integrating, an expression for the intrinsic softening modulus $\widehat{H}_0$ is finally achieved:

$$\widehat{H}_0 = -\frac{c_0^2}{2\mathcal{G}_f^{(dct)}} \frac{2\tilde{m}^2 - \gamma\tilde{m} + \gamma}{\tilde{m}}. \tag{69}$$

Substituting empirical laws (45) and (21) into Eq. (69), we finally get an expression for the intrinsic softening parameter in terms of the internal hardening variable:

$$\left|\widehat{H}_0(\xi^h)\right| = \frac{\eta_0}{\xi^h} A_H e^{B_H \xi^h}, \tag{70}$$

where

$$A_H = \frac{2(\tilde{m}^2 - \gamma\tilde{m} + \gamma)}{3\tilde{m}} \frac{A_{c_h}^2}{A_{\mathcal{G}_f}}, \tag{71}$$

$$B_H = 2B_{c_h} - B_{\mathcal{G}_f}. \tag{72}$$

In Fig. 9, relation (70) between the intrinsic softening parameter $|\widehat{H}_0|$ and ξ^h is plotted. The graph shows that $\widehat{H}_0$ is close to zero for the range of low densities. This means that the softening mechanism is not active at low densities. This observation is consistent with experimental facts: in the early stages of the pressing, densification takes place principally by rearrangement of the powder particles (Fleck, 1995), and therefore the body does not possess a significant cohesive strength. This lack of adhesion of powder particles renders the role of softening, interpreted as deterioration of strength, meaningless in this particular situation, because there are no measurable strength to be degraded.

A noteworthy feature of the present approach is the hypothesis presented above by which the intrinsic softening parameter $\widehat{H}_0$ is regarded as a state variable. The lack of experimental data concerning fracture energy in other fracture tests precludes the possibility of strictly corroborating this certainly debatable hypothesis. Nevertheless, it would be instructive to briefly examine and put on a quantitative basis the consequences of such a proviso. For this purpose, consider a *compression* test characterized by a stress path during plastic loading given by $q = -\sqrt{6}p$.[15] For a typical value $\gamma = 0.01$ of the dilatational coefficient and a parameter of internal friction $\alpha = 2.29$, we get:

$$\widehat{H}_0 = -15.8 \frac{c_0^2}{2\mathcal{G}_f^{(ct)}}. \tag{73}$$

where $\mathcal{G}_f^{(ct)}$ stands for the fracture energy associated to a uniaxial compression test. The same operations for a uniaxial tensile test yields:

$$\widehat{H}_0 = -0.52 \frac{c_0^2}{2\mathcal{G}_f^{(tt)}}. \tag{74}$$

In view of Eqs. (73) and (74), the fracture energy measured in a uniaxial compression test would be $15.8/0.52 \approx 30$ times greater that the one linked to the one obtained in a uniaxial tensile test. For other granular media, such as concrete, this ratio gives approximately 100 (Oller, 1998).

3. Numerical implementation

Although the thorough treatment of issues pertaining to the numerical implementation of the model is not the goal of this work, it is convenient to, before launching into details of the validation of the model, provide an abridged overview of some aspects that may result crucial for acquiring a proper grasp of the ensuing computed results; for a more detailed account, the reader is referred to Hernández (2009).

The algorithm used for integrating the constitutive differential equations is the so-called *Impl-Ex* scheme, originally proposed by Oliver et al. (2006), and further elaborated in Oliver et al. (2008), to improve the robustness of implicit algorithms in the numerical simulation of material failure. Oliver et al. coined the term *Impl-Ex* (*IMPLicit-EXplicit*) to suggest that the method shares some of the features of both implicit and explicit integration schemes. Roughly, the essence of the method is to solve *explicitly* for some variables, in the sense that the values at the beginning of the increment are presumed known, and *implicitly* for other group of variables. The main motivation behind the use of this non-conventional integration method is to avoid the adverse effects, exhibited typically by fully implicit, standard integration schemes (Belytschko and Mish, 2001), of softening-induced non-positive definite algorithmic elasto-plastic moduli. This methodology, in turn, entails the solution at each time increment of the non-linear system of equations stemming from the implicit backward-Euler difference scheme, i.e. the so-called *return-mapping* equations, since the above mentioned group of "explicit" variables are but *extrapolated values* of the same quantities computed *implicitly* at previous time steps.

In regard to finite element approximation, an updated lagrangian viewpoint has been adopted for describing the motion of the mesh, with a mesh update procedure based on the so-called Particle

Finite Element Method (PFEM) (see Oliver et al., 2007).[16] This method imposes a limitation concerning element technology: finite elements are to be *three-nodes triangular elements* (linear). To avoid the acclaimed inaccuracies that may emerge in the response in using such simple finite elements (e.g. *locking*), a finite element approximation based on a mixed variational formulation, with displacements and pressure as basic variables, and continuous linear interpolation for both fields, has been implemented.[17] The formulation has been specialized to address plane strain and axisymmetric problems.[18] The localization bandwidth at each quadrature point (see Section 2.7) is calculated as $l_f = \sqrt{2A_e}$, where A_e is the area of the corresponding triangular element. Tools are modeled as elastic bodies undergoing small deformations. Powder-tool contact conditions in the normal direction are imposed as a pure geometrical constraint; two different strategies are used to treat numerically such constraint, namely, the penalty method and the augmented Lagrangian strategy (used in more accuracy-demanding situations). To account for the fact that the powder becomes stiffer as densification progresses, a density dependent penalty parameter is employed when using the penalty strategy. Constitutive behavior in the tangent contact direction is characterized by the corresponding dry friction coefficient; following Oliver et al. (2007, 2009), Hartmann et al. (2009), interacting portions of contacting bodies are identified via an interface mesh.

4. Results

4.1. Diametral compression test

The *quantitative* assessment of the computed results is carried out by recourse to a common fracture test: the Brazilian or diametral compression test. The experimental data have been obtained from Jonsén et al. (2007,).[19] These experimental works include a detailed pictorial description of the crack development, as well as relevant quantities concerning the characterization of fracture, such as tensile strength and fracture energy, for several densities (ranging from 4.90 to 7.35 g/cm³). The numerical simulations presented here correspond to a specimen of final average density $\rho = 7.21$ g/cm³. Specifically, load data corresponding to this density level are given in Jonsén and Häggblad (2007).

A schematic description of the experimental setup is shown in Fig. 10. Force is applied over two diametrically opposite arcs of angular width $2\alpha_B = 14°$. The fixture tools are modeled as elastic bodies, with Young's modulus $E_{\text{tool}} = 2.1 \ 10^5$ MPa and Poisson's coefficient $\gamma = 0.3$. The specimen is compacted by single-action pressing of an iron based Distaloy AE powder. The apparent density of the powder is 3.10 g/cm³, and the full green density 7.48 g/cm³. An uniform density distribution is assumed, as the only

---

[15] The ratio q/p is not linear in a compression test after bifurcation, since important shear stresses develop at the localization band Lubliner (1990) (fracture occurs under *shear mode* or mode II conditions and, consequently, the hypothesis of uniaxial stress state is no longer valid). However, the approximation adopted here $q/p = -\sqrt{6}$ (the same path traced during elastic loading) serves as a first approximation for estimating the fracture energy associated to this test.
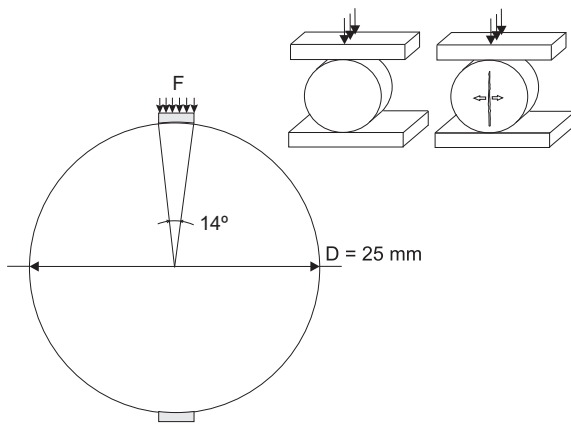
[16] This mesh update is only needed in the simulation of the pressing stage. During the subsequent pressure release and ejection stages, finite elements are not severely distorted (small strain regime).

[17] For details on the implementation procedure for the employed mixed formulation, the reader is referred to Agelet de Saracibar et al. (2006, 2004).

[18] No *practical* applications of powder compaction occurs under plane stress conditions. When needed, the plane stress constraint can be imposed (exactly in the elastic range and *approximately* in the plastic one) by an appropriate conversion of the elastic constants Belytschko et al. (2001).

[19] Incidentally, note that these experimental data are the same employed in Section 2.7 to calibrate the softening law. In doing so, we are, apparently, violating a well-known precept of numerical modeling: experimental data used for calibrating a model should not be employed also for its validation. However, the observance of this rule is only strictly necessary when the connection between overall strain and stress measures is direct, as in the characterization of the hardening response. By contrast, the derivation of the softening law is not direct, due to the localization of strains, and a host of assumptions is implied in relating the decrease of cohesion (stress measure) in the zone affected by the cracking process and the accumulated inelastic shear deformation (strain measure). Thus, the use of the same test for validating the model can be viewed as a legitimate means of critically evaluate these assumptions.
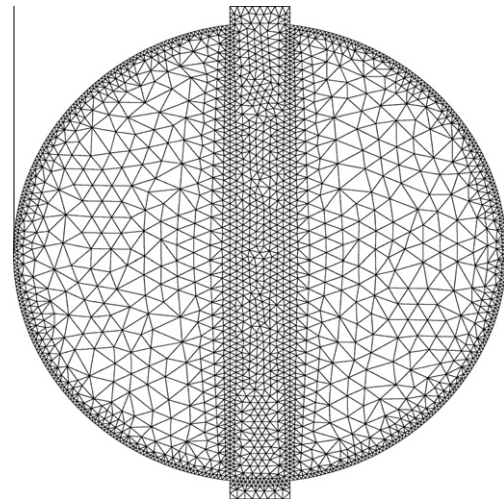
Fig. 10. Diametral compression test.

Fig. 11. Mesh layout.

information provided in this regard is the final average density (ρ_0 = 7.21 g/cm^3) of the compacted specimen. The final dimensions are D = 25 mm and t = 5 mm, where D denotes the diameter and t the height of the cylindrical specimen. According to Doremus et al. (2001), these dimensions (t/D = 0.2) ensure that the proviso plane stress can be employed to analyze the stress state during the experiment. For simulating the experiment, a vertical displacement of 0.2 mm is prescribed upon the top face of the upper fixture tool.

As regards to material properties, the yielding mechanism is characterized by an initial cohesion c = 29.9 MPa and an internal friction parameter α = 2.2. These values follow from the curve-fitting equations derived in Section 2 by simply setting the internal hardening parameter to $\xi^h \approx \eta$ = 7.21/7.48 = 0.96.

As mentioned earlier, the characterization of the elastic response is a somewhat controversial issue. Two empirical relations were presented in Section 2.3 for the Young's modulus as a function of relative density (internal hardening variable) (see Eqs. (14) and (15)). Evaluation of the former, the one advocated by Pavier (1998), at ξ^h = 0.96 yields E^e = 168444.0 MPa, whereas the linear relation proposed by Coube (1998), on the basis of measurements of the velocity of sound on an unstressed specimen (Eq. (15)), gives E^e = 21127.0 MPa. The consequences of using one or the other relation will be properly assessed later. Other relevant material parameters are the Poisson's coefficient (ν^e = 0.29) and the intrinsic softening modulus, which can be obtained from the graph shown in Fig. 9, giving $\hat{H}_0 = 9.0 \cdot 10^5$ MPa/mm. The dilatancy factor γ is set to 0.01.

4.1.1. Numerical aspects

Prior to compare the experimental results with the calculated response, it is expedient to examine the sensitivity of the numerical results to subsequent mesh refinement. The mesh layouts[20] used in this analysis are patterned after the non-uniform mesh depicted in Fig. 11; the higher mesh density in the vertical central band is dictated by foresight of the fact that the dominant crack will be located along the loaded diameter. Five different meshes characterized by the size of the elements h in this central band are used. Young's Modulus is set to E^e = 21127.0 MPa, and the time domain is discretized into 800 equally spaced intervals. The analysis is carried out by examining $F - \nu$ plots: the vertical deflection ν corresponds to the displacement prescribed upon the nodes located at the top face of

the fixture tool; the applied load F is obtained as the sum of the forces at these nodes.

Computed results are shown in Fig. 12. As far as the magnitude of the peak value of the load is concerned, the sequence of graphs displayed in Fig. 12 exhibits clear convergence with refinement of the mesh. The peak value predicted by using the mesh labelled as h = 0.4 mm is only a 0.6% lower than the one obtained with the coarser mesh h = 0.6 mm. On the other hand, the magnitude of the "residual force" – the force calculated at the onset of the post-peak ascending branch – ranges between 2.85 and 2.91 kN, although without a clear monotonic convergence tendency. In view of these circumstances, it seems that going to finer discretizations will not improve significantly the accuracy. Hence, the mesh labelled as h = 0.4 mm, which corresponds to the one displayed in Fig. 11, will be taken as the finite element mesh for the simulations shown in the sequel.

These sequence of force versus displacement diagrams presented in Fig. 12 indicates that the energy[21] dissipated during the loading process apparently converges as the mesh is refined. As alluded to in Section 2.7, lack of convergence upon refinement of the finite mesh is one of the flaws that plague the numerical treatment of models exhibiting strain-softening behavior. Thus, it seems that, at least in this example, the employed regularization of the softening law has proved useful in alleviating this problem.

4.1.2. Computed versus experimental results

4.1.2.1. Quantitative results. We are now in the position to compare the computed response (using N = 800 steps, typical mesh size h = 0.4 mm) with experimental results. The plots of the computed force versus vertical deflection for two distinct Young's modulus E^e = 168444.0 MPa and E^e = 21127.0 MPa, in conjunction with the corresponding experimental curve, provided by Jonsén and Häggblad (2007), are depicted in Fig. 13. This diagram clearly shows that the Young's modulus estimation E^e = 168444.0 MPa, obtained from triaxial measurements (Pavier, 1998), is utterly inadequate for characterizing the elastic response of the green compact under the conditions of this diametral compression test, being more appropriate the estimation E^e = 21127.0 MPa, derived from ultrasound tests (Coube, 1998). Nonetheless, even in this case, significant differences with experimental data are observed, as we detail in what follows. The slope of the numerical $F - \nu$

---

[20] Care is to be exercised in selecting the mesh size in the region where the load is applied to the specimen, since excessively coarse meshes may not represent adequately the stress concentration, leading to a mechanism of failure different from that of cracking along the loaded diameter.

[21] Recall (see Fig. 8) that the energy dissipated can be estimated in terms of the area enclosed by the force displacement graphs of unsplit and split tests.
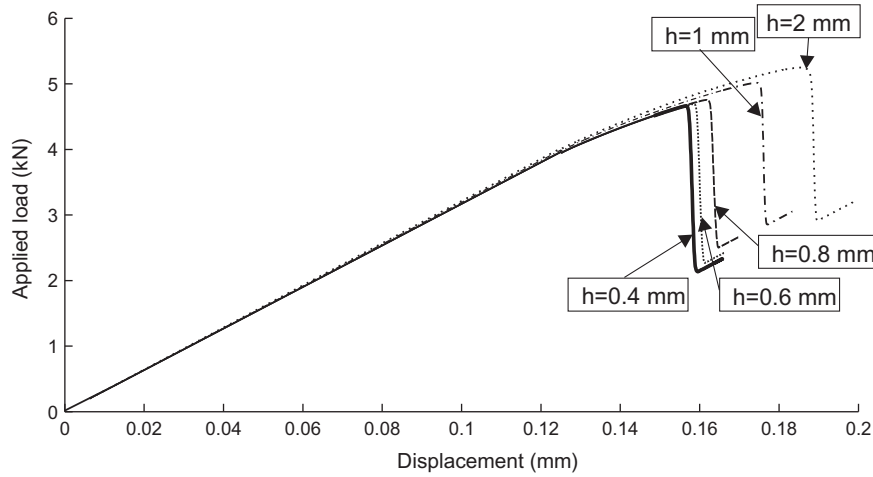
Fig. 12. Applied load against deflection. Result for several meshes, characterized by the size h of their elements.
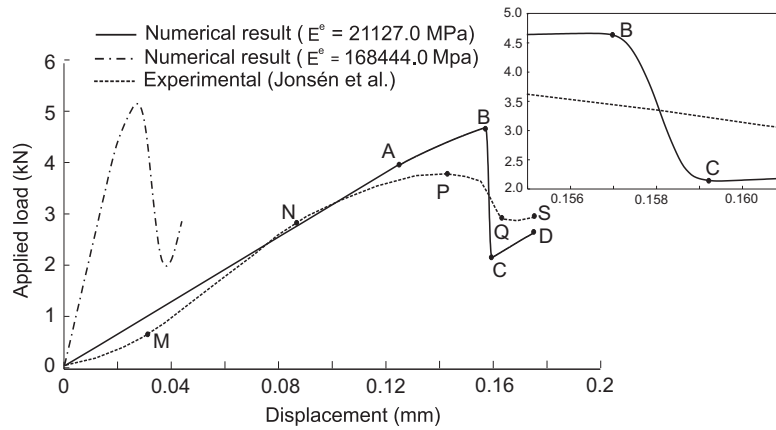

Fig. 13. Applied load versus deflection. Comparison of computed results using different elastic properties with experimental data collected by Jonsén and Häggblad (2007). The post-peak descending branch B–C is shown in magnified form.

graph remains constant until point A; by contrast, the plot of the experimental force versus deflection traces initially a non-linear path OM. Then, it becomes linear up to the point N, at which, according to Jonsén and Häggblad (2007), the elastic nature of the graph ceases due to the initiation of the central crack. These markedly distinct elastic responses highlights, again, concern with the characterization of the elastic response, which should receive clearly more careful consideration in future improvements of the model.

The progressive decrease in slope observed experimentally (path NP) during crack growth is more pronounced that the decrease in slope predicted by the model (path AB), which is practically unnoticeable. As a consequence, the computed peak load (point B) exceeds in 20% the maximum force measured experimentally (point P), and the displacement at which this peak is reached, is overpredicted in 11%, amounts that, albeit apparently unduly large, are within a reasonable range of accuracy if we consider the significant uncertainty (10–15%) attached to the experimental determination of tensile properties in green compacts.[22]

Discrepancies in the post-peak behavior are also noteworthy. In the experiment, a relatively gradual decay of load is recorded (path PQ), whereas this decay occurs precipitously, although not instantaneously[23] (path BC in the simulated response), resulting a residual force underestimated by approximately 30%, and thus, an overestimation of the dissipated energy.

These differences between observed and calculated (pre-peak and post-peak) responses may be rationalized as due to the numerous simplifying assumptions made in Section 2.7 in deriving the softening law. Such assumptions, although physically plausible, have no experimental corroboration and thus are arguable. Another contributor to these discrepancies may be found in the elementary character of our crack modeling approach, which does not provide any means to "track" the propagation of the forming cracks. Indeed, the post-peak portion of the curve corresponds to the unstable growth of the central dominant crack. Without a proper tracking algorithm, the localization band may tend to follow certain preferred directions dictated by the mesh, giving rises to spurious "crack branching". An immediate implication of such spurious branching is that the extent of the region affected by loss

---

[22] The material parameter that has more influence in the location of the peak load is the cohesion variable (c). Note that the experimental values for cohesion shown in Section 2 are *derived data* (Broek, 1988), in the sense that they are obtained from *raw data* (tensile and compression strength, for instance) through an interpretation process full of assumptions. Thus, in addition to the error involved in obtaining the *raw data*, one has to acknowledge the uncertainty associated to such assumptions.

[23] The enlarged view of path BC, shown in the upper-right part of Fig. 13, reveals several time steps are required in its computation. An instantaneous drop would have corresponded to a *perfectly brittle response*. A force versus displacement graph that exhibits such feature warns of trouble with potential *snap-back behavior* (Crisfield, 1991).
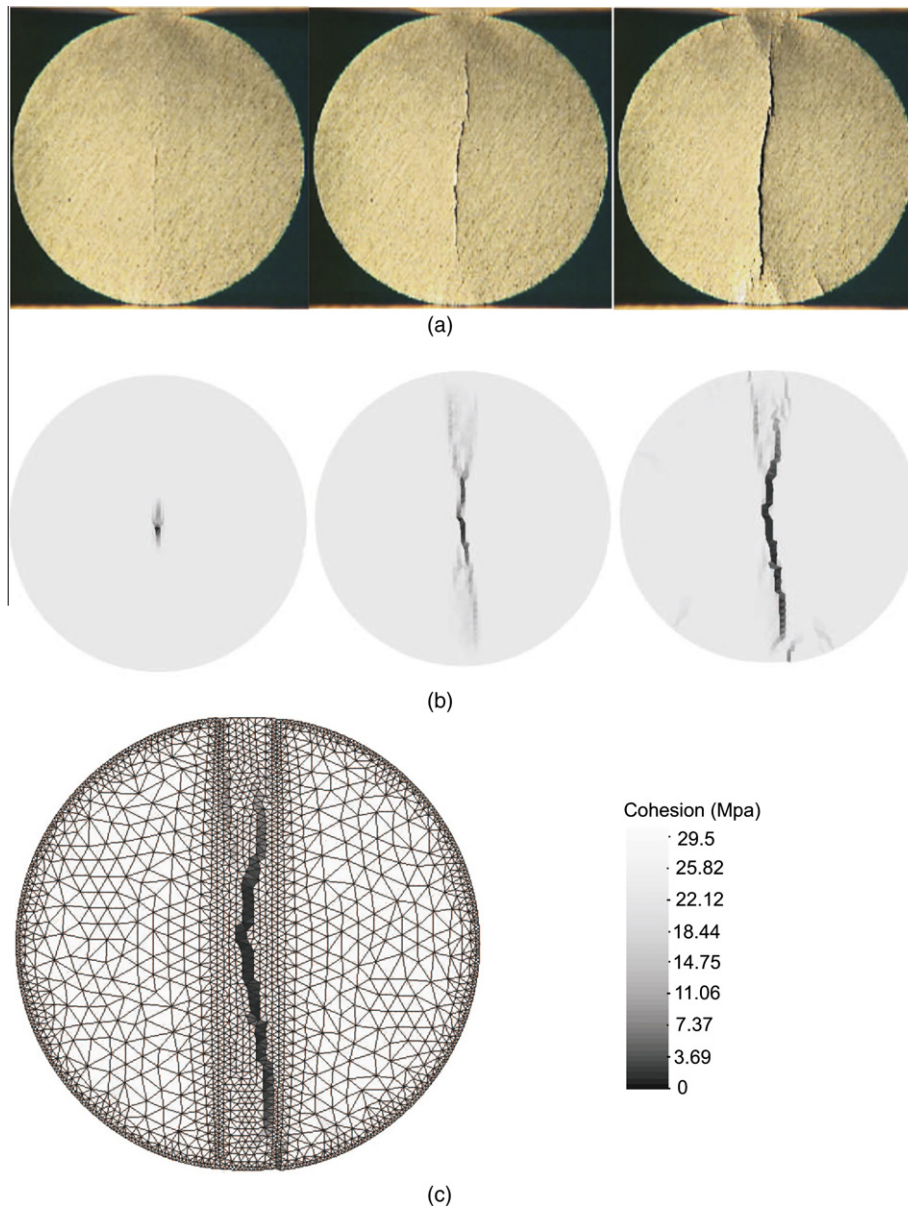
Fig. 14. (a) Images recorded experimentally by Jonsén et al. (2007): initiation of the crack, point of maximum load, and end of the loading process. (b) Contour plots of computed cohesion corresponding to such stages. (c) Contour plot of computed cohesion at the end of the loading process, showing the spatial grid used in the computation.

of cohesion increases, and so does, hence, the dissipated energy. Last but not least, it is well-known that fracture tensile tests on granular materials are unduly sensitive to test conditions. Aside from deficiencies in both the material constitutive model and the numerical solution algorithm, thus, discrepancies may be also the manifestation of inadequate modeling of such test conditions; accounting for the actual stiffness[24] of the testing frame, for instance, is crucial to adequately capture the post-peak behavior (see e.g. Lubliner, 1990).

4.1.2.2. Qualitative results. Fig. 14(a) contains images recorded experimentally by Jonsén et al. (2007) during the loading process. The leftmost picture corresponds to the initiation of the crack at the center of the disc (point N in the $F - v$ curve shown in Fig. 13). The central image shows the state of the crack at the point of maximum load (point *P* in Fig. 13). Finally, the rightmost picture

displays the aspect of the crack at the end of the loading process (point S in Fig. 13). Aside from the central "dominant" crack, secondary cracks are distinguishable around the contact zones.

Cracks impair strength. Thus, a natural way of representing such defects is by plotting *contours of cohesion* (green strength), in which crack locations are identified as those areas affected by a *local decrease of cohesion*. The corresponding sequence (initiation of the central crack, maximum load and end of the test) of computed contour plots of cohesion is shown in Fig. 14(b). In the leftmost plot, the local decay of cohesion observed in the center of the disc indicates the initiation of the crack. In the central contour plot (maximum load), we can see that this loss of cohesion propagates to the periphery of the disc along the loaded diameter. Close to the center of the disc, this propagation occurs along a single path. Near the loading surface, however, the de-cohesion path seems to bifurcate into two branches. Such bifurcation (or "crack branching") is not detected in the experiment. Inspection of the rightmost plot (end of the test), indicates that, eventually, loss of cohesion has been more intense along one of these branches. Interestingly, the

---

[24] The work by Jonsén et al. (2007) does not provide information concerning such a feature.

resulting "dominant" path, which spans approximately 80% of the length of the diameter, displays a distinctly crack-like appearance, and bears close similarity with the crack observed in the corresponding photograph. Note that other regions with relatively low cohesion, located mainly around the contact zones, are discernable in the final contour plot. The aspect of these patterns of low cohesion are in remarkable agreement with the abovementioned secondary cracks detected experimentally. In Fig. 14(c), the final cohesion contour is plotted in conjunction with the finite element mesh used for the computation. This plot allows us to distinguish the band of elements along which loss of strength is *localized*.

4.2. Pressing and ejection of a thin cylindrical part

The simulation of the *pressing and ejection of a thin cylindrical part* seeks to highlight the usefullness of the numerical model in reinforcing the physical understanding of how well-known crack typologies are developed. In addition, this simple example typifies perfectly the process of compaction, since it touches upon all the relevant issues: pressing, axial unloading, ejection, radial springback, development of cracks, etc. The experimental data to validate this test have been obtained from the extensive crack database collected by Zenger and Cai (1997). It should be pointed out that, in contrast to the diametral compression test shown previously, this simulation is intended to provide only a *qualitative assessment* of the model's ability to reproduce crack formation.

A cylindrical part made of an iron based Distaloy AE powder, with apparent density $\rho_{app} = \rho_0 = 3.04$ g/cm^3 and theoretical density ρth = 7.33 g/cm^3 is pressed until reaching a final density $\rho = 7.18$ g/cm^3. The punches and the die are considered elastic materials characterized by a Young's modulus $E_{tool} = 210000$ MPa and a Poisson's ratio $v_{tool} = 0.3$. Their dimensions are displayed in Fig. 15.

The motion of the upper and lower punches is controlled by prescribing vertical displacements on its top and bottom surfaces, respectively. During pressing, the upper punch moves downward with constant velocity 10 mm/s while the lower punch and the die remain stationary. Release of axial pressure takes place at a rate 20 mm/s by gradually lifting the upper punch. During ejection from the die, the lower punch pushes the compact upward at a constant rate 40 mm/s. This example focuses on the prediction and description of cracks formed due exclusively to *elastic expansion of the compact upon exiting the die*; contribution of friction effects to the occurrence of cracks will be hence ignored by setting the friction coefficient to a low constant value $\mu = 0.01$. Material parameters are obtained from the calibration presented in Section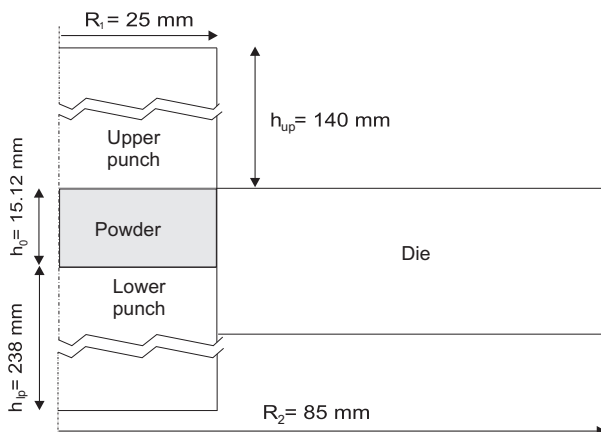 2. From the two alternative empirical relationships for the Young's modulus given there, we shall use the one advocated by Pavier (1998), see Eq. (14).

The initial finite element mesh is shown in Fig. 16. The average size of the elements of the powder body is $l_e = 1$ mm, whereas the size of the elements at the boundaries of punches and die in contact with the powder is, approximately, 0.5 mm.

4.2.1. Assessment of the crack prediction methodology

We consider first the case corresponding to an ejection with total removal of the upper punch followed by an upward movement of the lower punch. Fig. 17.a contains a sequence of three contour plots of cohesion during this ejection process. In the leftmost plot, the compact is still confined within the die cavity. It follows from the uniformity exhibited by the cohesion distribution that the green strength has not been altered and remains at the same value attained at the end of the pressing stage. In the central plot, almost one half of the compact has already emerged from the die. To make more distinguishable changes in cohesion, this plot is displayed in magnified form in Fig. 17(b) with a narrower grayscale. A de-cohesion pattern, in the form of darker "spots", is observed along the emerged portion of lateral surface. This mechanical damage is apparently superficial, since only the outer layer of elements is appreciably affected by loss of cohesion.

The rightmost plot of Fig. 17(a) is the cohesion contour map at a point where 85% of the upper portion of the part is clear of the die. An enlarged view of such plot is displayed in 17(c). In addition to the above mentioned lateral de-cohesion pattern, which has progressed along the perimeter, decrease in cohesion is detected at the upper half portion of the part. The degradation is more intense along the upper layer of elements. Near the axis, the resulting decay is estimated in 95% of the value of cohesion attained at the end of the pressing stage. As we move downward, the intensity of the degradation diminishes gradually and becomes more diffuse.

Fig. 17.d shows schematic descriptions of two type of crack patterns observed experimentally in *Class I parts*. These sample crack layouts have been obtained from the almost exhaustive crack database elaborated by Zenger and Cai (1997). The agreement with experimental evidences becomes qualitatively apparent by simply comparing the computed contour plots with these schematic descriptions. The mechanical deterioration observed on the lateral surface appears due to the absence of a smooth taper to allow some
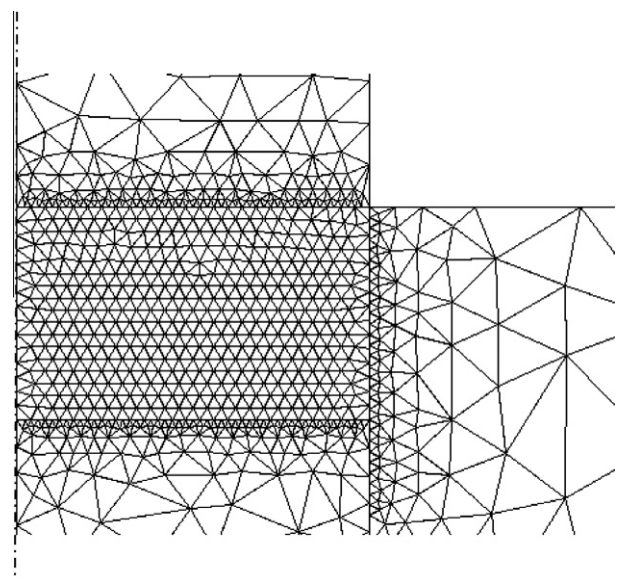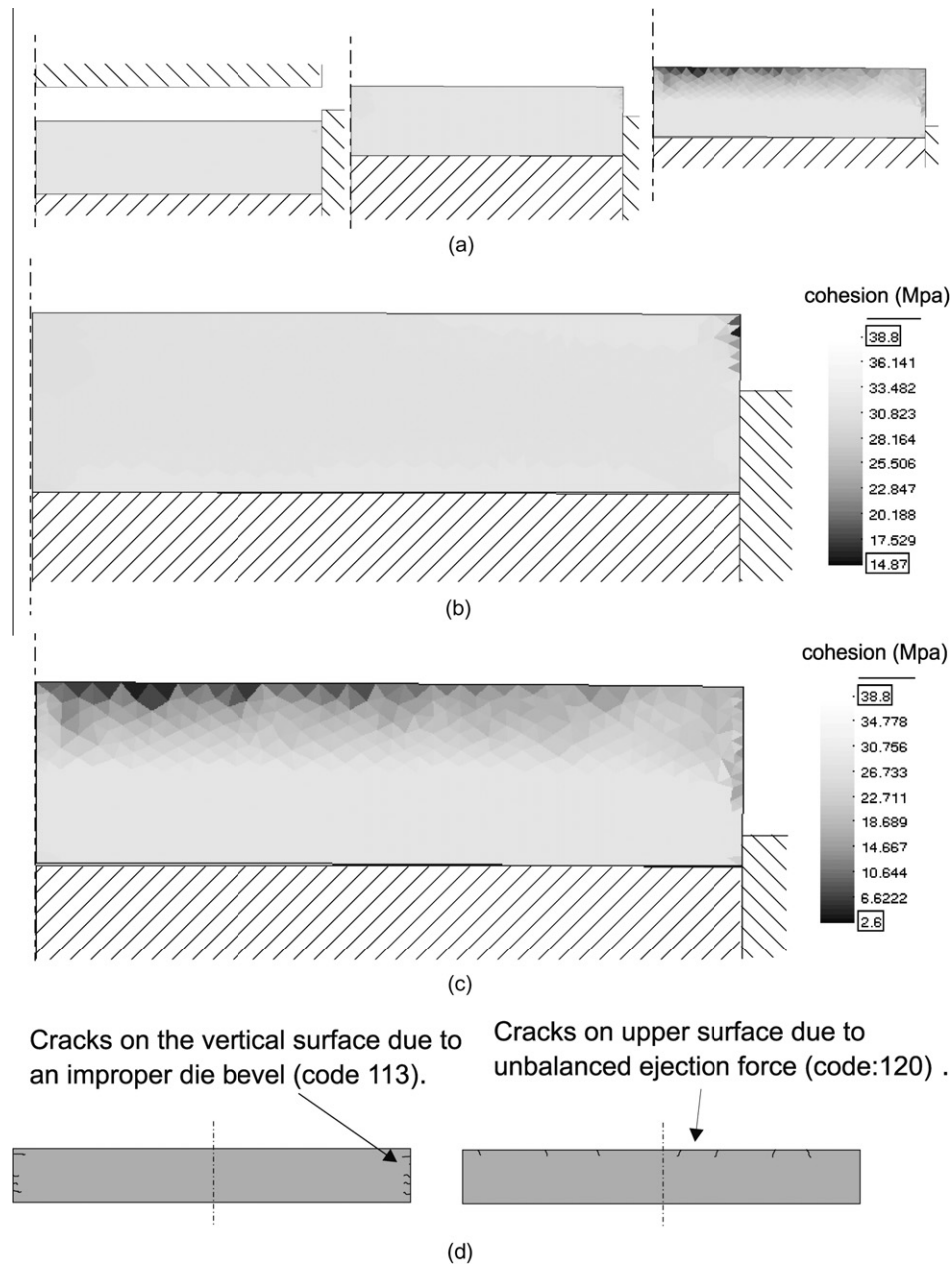

Fig. 15. Dimensions of punches and initial die cavity.

Fig. 16. Initial mesh layout.

Fig. 17. (a) Contour plots of computed cohesion during emergence of the compact from the die. The central and rightmost plots are displayed in magnified form in (b) and (c), respectively. (d) Qualitative description of cracks observed in thin parts reported in the database of common cracks collected by Zenger and Cai (1997).

degree of radial relaxation; the other typology of failure, the one detected on the top surface, is almost ubiquitous in the ejection of Class I parts (Zenger and Cai, 1997), and is caused by bending stresses, as illustrated in Fig. 18.

The non-homogeneity of the computed cohesion distribution indicates that the mechanisms of strain softening have been certainly activated. Elements of the lateral and upper surface at which the cohesion is markedly lower may be loosely interpreted as locations of *macroscopic cracks*. However, the de-cohesion patterns shown above do not exhibit, certainly, a distinctly crack-like appearance, if compared, for example, with the results depicted in Fig. 14. A reason that may explain this apparently "poor" representation may be that the finite mesh employed in the calculations (see Fig. 18(b)) is too coarse for adequately capturing localization of plastic strains. To corroborate this, an analysis with a finer mesh has been carried out. The alternative mesh is shown in Fig. 19(a).

The typical element size has been set to approximately 0.15 mm, which results in almost 10000 elements only for the body powder, in contrast with the 1000 elements of the mesh displayed in Fig. 18(b). The aim is not to examine the compaction process in its entirety, but merely to evaluate the ability of the model in replicating the flexural cracks appearing on the horizontal top surface. For simplicity, thus, the effect of the die has been replaced by prescribed lateral pressure (200 MPa) acting on the lower fourth of the part. The corresponding contour plot of computed cohesion is shown in Fig. 19(b). Loss of cohesion is more accentuated along three (on each half) easily discernable vertical paths emanating from the top surface of the part, which, in turn, implies that localization of plastic strain has indeed taken place.

The hypothesis advanced previously seems thus to be sustained: a finer mesh ensures a more "pleasing" and realistic aspect. However, it should be stressed again that the ultimate goal of the
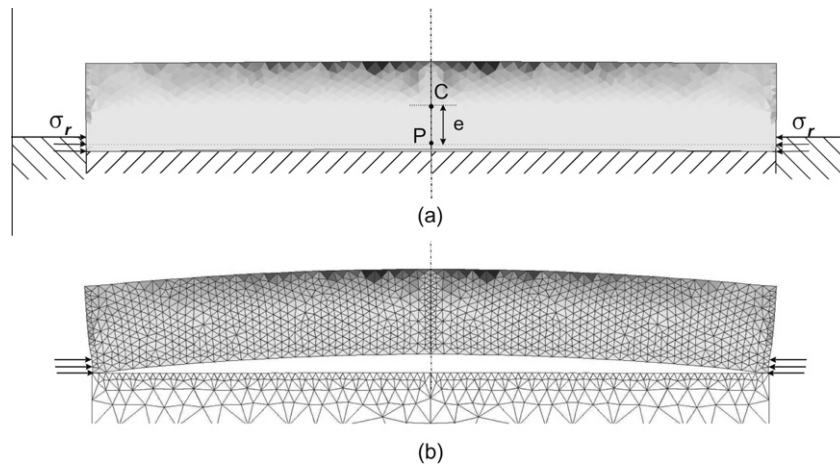
Fig. 18. (a) Eccentricity of the resultant of lateral stresses causes bending of the part. (b) Deflected shape showing the finite element mesh in the simulated part (displacements scaled up 10 times).
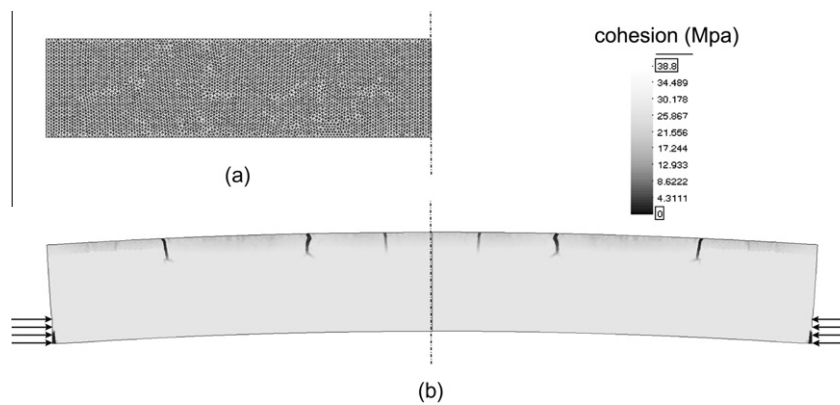

Fig. 19. Dieless case: (a) overly refined mesh, (b) contour plot of cohesion with displacements scaled up 10 times.

results provided by the numerical model is to ascertain whether a given fabrication route will lead to defective parts or not. The model should have the capability of predicting the formation of macroscopic cracks, but without the need of giving an accurate description. From the contour plots of cohesion obtained with the coarser mesh shown in Fig. 18(b), one can conceivably conclude that, in this case, the ejection schedule with total axial unloading will lead invariably to defective parts due to tensile stresses induced by bending. The exact dimensions of these bending cracks and their exact distribution over the upper surface are of little concern. Consequently, going to unduly fine meshes, as the one displayed in Fig. 19(a), is inefficient from a practical point of view. Too many refinements in engineering solutions pertain to secondary errors; they increase the complexity, but do not improve the solution.

4.2.1.1. Analysis of the process in the mean-deviatoric stress plane. In order to disclose in full the nature of the phenomenological events (hardening, softening and elastic behavior) that takes place during the process, it proves instructive to plot in the mean-deviatoric stress plane the stress history at a representative point together with the respective sequence of surfaces defining the yield condition. Fig. 20(a) represents the stress evolution at a node located close to the upper face of the part. During the pressing stage, the stress state traces the path *AB*. The monotonically increasing character of this loading history ensures that the powder is always at yielding during this phase. The strength of the material thus raises

progressively, and this hardening behavior is indicated by the expanding yield surfaces (dashed lines). The yield surfaces drawn with a solid line represents the yield condition at the end of the pressing stage. Within the region enclosed by these yield surfaces, the behavior of the material is presumed to be elastic.

During axial unloading, the stress state follows a piecewise approximated linear path *BCD*; the yield condition is not affected during this phase, since the entire trajectory lies within the elastic region and, thus, mechanical properties are not altered. By definition, the deviatoric stress measure q^* must remain positive. Thereby, the descending tendency of the stress trajectory breaks down at point C, at which the trajectory is "reflected"; the slopes (in absolute value) of the descending and ascending branches are consequently identical. Point *C* corresponds to a hydrostatic stress state and it marks[25] the transition to stress states in which the radial pressure is dominant ($\sigma_r > \sigma_z$). At point *D*, the axial pressure exerted by the upper punch is totally released.

The removal of the upper punch is followed by the upward movement of the lower punch for ejecting the part out of the die. As the part moves toward the die exit, the radial stress at the analyzed material point diminishes gradually; this elastic unloading process is represented by the descending path *DE* in

---

[25] Due to the deliberately low value of the friction coefficient, shear stresses are negligible and radial stresses are approximately constant along the radial direction. Hence radial and hoop stresses are identical, and the deviatoric stress measure can be expressed simply as $q^* = |\sigma_z - \sigma_r|$. Hence, $q^* = 0$ implies $\sigma_z = \sigma_r$.
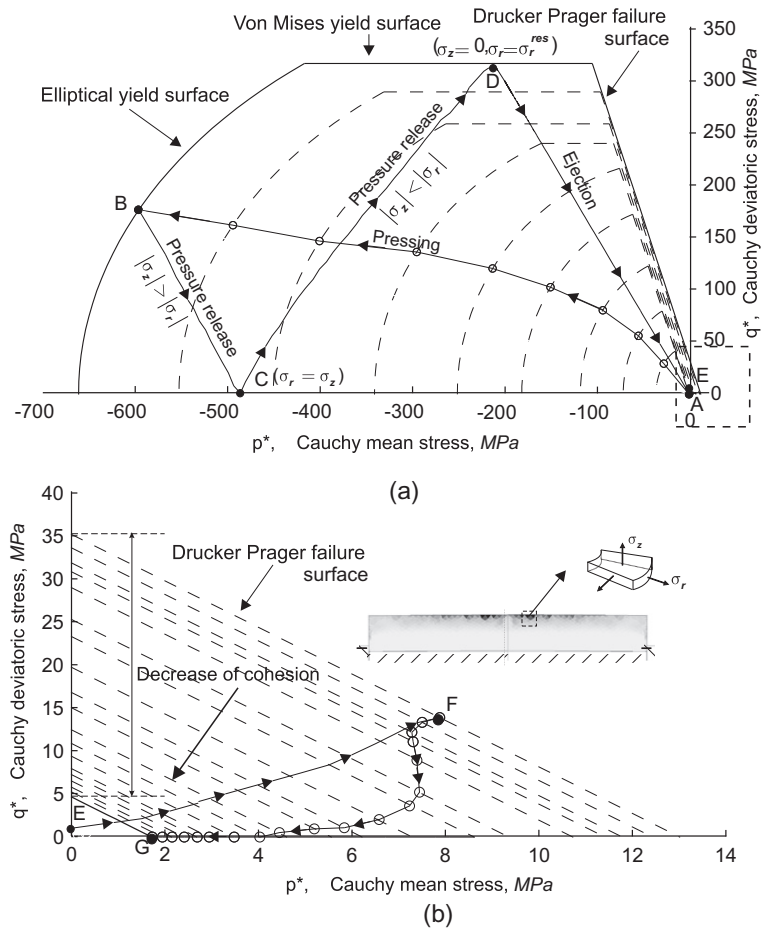
Fig. 20. Stress trajectory in the mean-deviatoric stress plane of a point located on the top face of the part. (a) Pressing (path AB), release of axial load (path BCD) and ejection (up to the onset of bending, path DE). (b) Enlarged view of the first quadrant. Path EF represents elastic loading due to tensile bending stresses. Path FG indicates decrease of cohesion (green strength) due to strain softening.

Fig. 20(a). When the analyzed point starts emerging from the die, the magnitude of the stress at this node practically vanishes, and the stress state remains thus close to the origin (point E). Ejection progresses and, when half of the part is out of the die, the eccentricity of the lateral force begins to produce the aforementioned bending deformation (see Fig. 18(b)). As a consequence, the upper portion of the part is stretched, hence put into tension. This bending deformation causes the stress state to move within the elastic tensile region (first quadrant of the mean-deviatoric stress plane), which is shown in magnified form in Fig. 20(b), until eventually reaching the Drucker–Prager failure line at point F. Yielding on this failure surface induces a decrease of cohesion (softening) of approximately 85%, from 35 to 5 MPa, and consequently, the Drucker–Prager failure line shifts toward the origin. This is illustrated graphically by the sequence of parallel dashed lines. During this continued yielding, the stress traces the path FG.

The usual industrial practice to prevent cracking caused by bending of the part is to maintain a certain level of axial load during ejection (Zenger and Cai, 1997). The upper punch must accompany the lower punch in its upward motion, "sandwiching" the part until it is completely out of the die cavity and thus avoiding the tendency to bend. The effect of the hold down pressure on the compact properties can be assessed properly in the mean-deviatoric stress plane. In Fig. 21, the stress evolution during axial unloading and ejection at the same material point analyzed previously (see Fig. 20), is drawn for several hold down pressures. The ejection branches HJ and BG correspond to total axial unloading

and 13% hold down pressure, respectively. In essence, the effect of keeping a certain level of axial load is reflected in the mean-deviatoric stress space as a translation of the unloading branch HJ, which shifts towards the compression side to BG; the final stress state moves far from the tensile region (first quadrant), thus avoiding the formation of tensile cracks. Needless to say, the larger the hold down pressure, the further the final stress will be from the tensile region (points E and F) and, consequently, the likelihood of tensile-type failure will decrease. However, large hold down pressures may promote other mechanism of failure, such as crushing. Furthermore, due to the concomitant increase of radial pressure, the deterioration of the lateral surface will be invariably aggravated.

4.3. Compaction of an axially symmetric multilevel adapter

We address now a more practical problem: the compaction of an axially symmetric *multilevel* adapter in an advanced computed numerically controlled (CNC) press machine. The geometry and dimensions of this part are displayed in Fig. 22. In view of the axial symmetry of both loading (pressing punches) and geometry,[26] the study is concentrated on a characteristic radial section. The initial die cavity dimensions and the mesh layout are shown also in

---

[26] Viewed in the light of the scope of our analysis, this simplification appears reasonable. Nevertheless, bear in mind that the propagation of cracks is inherently a three-dimensional phenomenon.
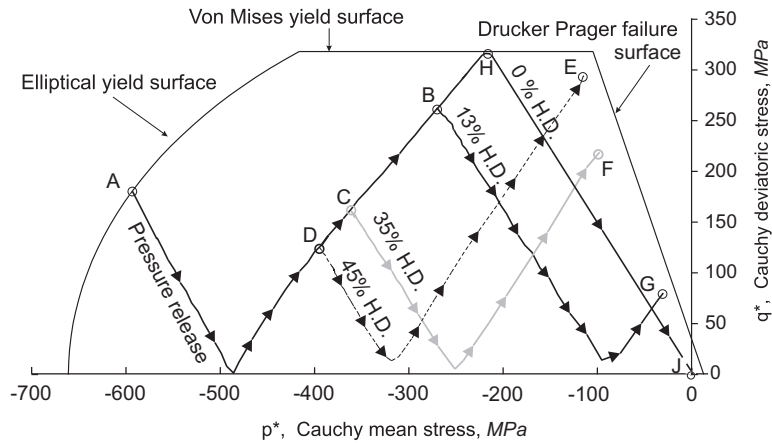
Fig. 21. Stress trajectories in the mean-deviatoric stress plane corresponding to ejection schedules with different hold down pressures.
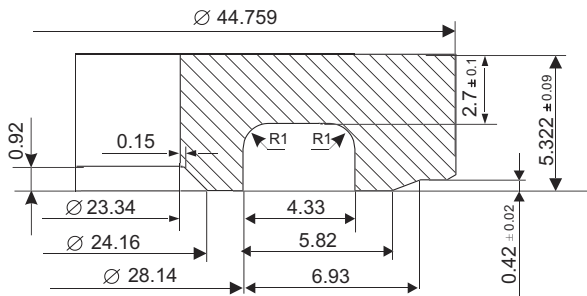

Fig. 22. Final geometry of the part (dimensions in mm).

Fig. 23. (a) Dimensions of the initial die cavity $\left(h_{LMP}^0 = 6.23 \text{ mm}, h_{LIP}^0 = 10.53 \text{ mm}, h_{LOP}^0 = 10.92 \text{ mm} \right)$. (b) Initial mesh layout.

Fig. 23. The average size of the elements of the powder body is $l_e = 0.25$ mm, whereas the size of the elements at the boundaries of punches and die in contact with the powder is, approximately, 0.15 mm; features on the bottom faces of the part demands smaller elements (≈ 0.05 mm) at these locations. The tool set employed to form the powder into the required shape comprises an upper punch (UP) of 126 mm height; three lower punches (LIP, LMP and LOP)[27] of heights 206, 150 and 87 mm, respectively; a die that controls the outer peripheral shape; and a core rod that controls the inner peripheral shape and size of the part. A glance at Fig. 23(b) allows

us to appreciate the striking contrast between the small volume occupied by the powder in relation with the dimensions of the pressing punches.

The powder employed in making the part is a Distaloy AE iron based powder with apparent density $\rho_{app} = 3.25$ g/cm³. Material parameters can be obtained thus from the empirical adjustment presented in Section 2. Fill density, which is assumed uniform throughtout the die cavity, is taken as the apparent density. Friction between the powder mass and the faces of the tools-die walls and core rod is modeled via a friction Coulomb law, with coefficient $\mu = 0.12$. The elastic behavior of the tooling is characterized by a Young's Modulus $E_{tool} = 210$ GPa and a Poisson's ratio $v_{tool} = 0.3$.

4.3.1. Pressing stage

It needs no emphasis that the success in predicting numerically the formation of cracks during the post-pressing stages (pressing release and ejection) relies considerably on the quality of the density and stress distributions computed at the end of the pressing stage. Thereby, we begin our analysis by comparing experimental – obtained by the Archimedes' method – and numerically calculated density values.

The effect of the mechanical and hydraulic drives of the advanced CNC press machine employed to shape the part are replaced by prescribed conditions on the top and lower faces of the upper punch and the lower punches, respectively. The upper punch is connected to a reciprocating mechanism during the pressing portion of the compaction cycle; the relation between the (vertical) displacement prescribed on the top of the upper punch and the position within the cycle exhibits thus a sinusoidal form, as shown in Fig. 24, and the pressing stroke u_{up} is given by the expression:
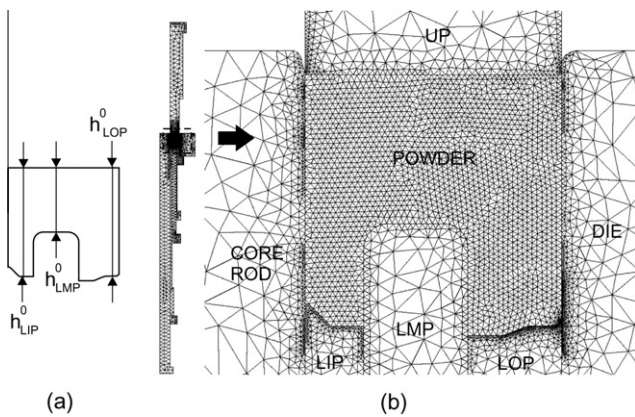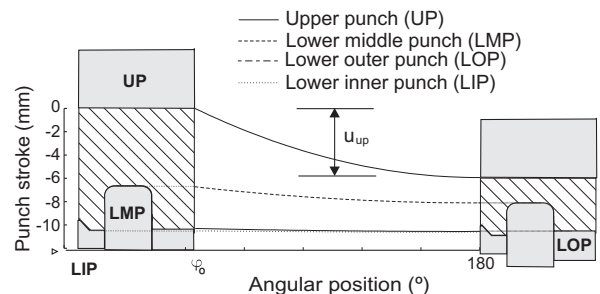

Fig. 24. Displacement profiles prescribed on punches during pressing stage. The angle φ_0 denotes the point in the cycle at which the upper punch enters the die cavity ($\varphi_0 = 157.3°$). The pressing stroke ends at $\varphi = 180°$ (bottom dead center).

---

[27] The acronyms LIP, LMP and LOP signify lower *inner* punch, lower *middle* punch and lower *outer* punch, respectively.

Table 1
Motion scale factors used for pressing the modified part.

	UP	LIP	LMP	LOP	DIE	CORE ROD
f	1	0.043	0.234	0.019	0.173	0.233
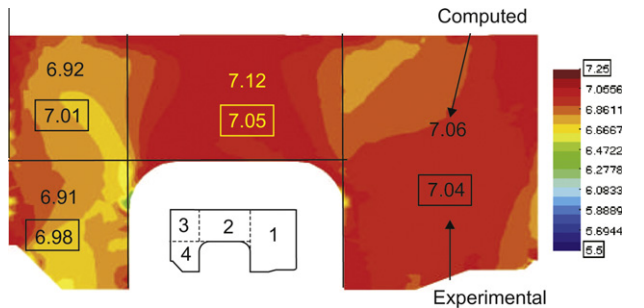
Fig. 25. Contour plot of density computed at the end of the pressing stage.

$$u_{up} = \left(1 - \sqrt{1 - \left(\frac{l_c}{l_r}\sin\varphi_0\right)^2}\right)l_r + (1 + \cos\varphi_0)l_c, \qquad (75)$$

where $l_c = 90$ mm and $l_r = 580$ mm – the lengths of the crank and the connecting rod, respectively. The velocity of the lower rams during pressing is kept proportional to the velocity of the upper ram, hence their motions also exhibit a sinusoidal profile, as can be readily appreciated in Fig. 24(a). The proportionality – or *motion scale – factors* for the case at hand are shown in Table 1.

Density contours corresponding to the end of pressing stage are shown in 25, accompanied by computed averaged density within the analyzed subdomains. These averaged values are compared with experimental measures in both Fig. 25 and Table 2. The density distribution obtained experimentally are clearly more uniform than the computed one. The maximum density is attained in the level formed by the lower middle punch; finite element analysis overestimates density in this region in 0.07 g/cm³. The portion with the lowest density is located above the lower inner punch; in this case, the numerically predicted value is 0.09 g/cm³ below the experimental one, which is also the maximum discrepancy between experiment and predicted density values. Since this error is, according to the powder modeling community (see PM Modnet Computer Modelling Group, 1999), within acceptable accuracy for density predictions (0.1 g/cm³), the agreement can be deemed satisfactory.
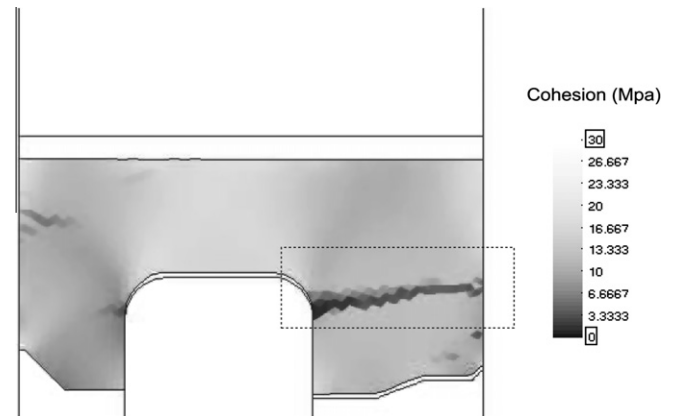
4.3.2. Pressure release

Using as starting point the above shown results obtained at the end of the pressing stage, we tackle now the analysis of the post-pressing operations. We concentrate exclusively on the simulation of the *pressure release* stage. In this stage, the upper punch moves upward a certain distance so as to reduce the level of axial and radial pressures, and hence facilitate the subsequent withdrawal of the die.[28] We consider here the extreme case in which the upper punch is lifted *completely* out of contact with the compact while the rest of tools remains stationary. To this end, a uniform displacement of 0.4 mm is prescribed on the top surface of the upper punch; the lower punches, the die and the core rod are kept fixed by imposing zero displacement on their bottom faces.

---

[28] The CNC press employed to consolidate the powder features a withdrawal-type tooling system, in which it is not the part that is pushed out from the compaction cavity while keeping fixed the die, as occurred, for instance in the case shown in Section 4.2, but rather the die is withdrawn whilst the compact remains stationary.

Table 2
Comparison between computed densities (ρ_{num}) and experimentally measured values (ρ_{exp}).

Zone	1	2	3	4	Overall
ρ_{num} (g/cm³)	7.07	7.12	6.91	6.92	7.04
ρ_{exp} (g/cm³)	7.04	7.05	6.98	7.01	7.03
$\rho_{num} - \rho_{exp}$ (g/cm³)	0.03	0.07	−0.07	−0.09	−0.01

Fig. 26. Contour plot of cohesion at the end of pressure release stage.

In Fig. 25, the computed contour plot of cohesion at the end of the pressure release stage is shown. Examination of this contour plot clearly reveals the existence of an horizontal de-cohesion pattern with a distinctly crack-like appearance. The evolution of this localized loss of cohesion can be appreciated in the sequence of contour plots displayed in 27. The crack emanates from the junction of the levels formed by the LMP and LIP. Then, it progressively propagates outward, in the horizontal direction, until reaching the periphery of the part. At the end of the pressure release stage, the computed de-cohesion path spans the whole section, a fact that suggests that separation of the lower outer skirt from the main web body may be imminent.

Fig. 27 contains the graphs of vertical displacement of the working ends of each punch as a function of the position within the compaction cycle. Since the bottom faces of the lower punches are kept fixed, these graphs provide information regarding punch
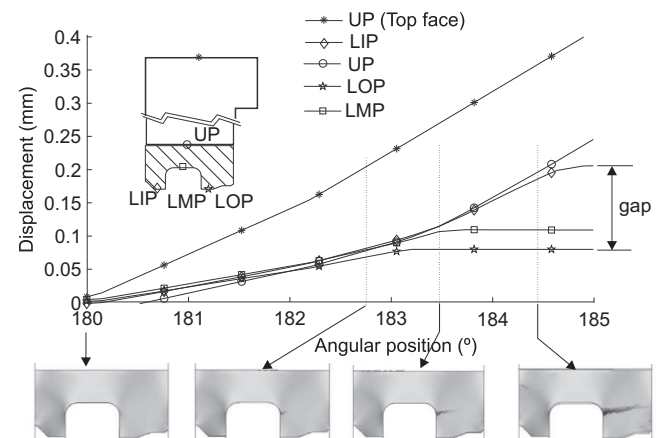
Fig. 27. (a) Displacement of the working ends of lower and upper punches, together with the displacement of the top face of the upper punch, as a function of the angular position. (b) Sequence of contour plots of cohesion.

deflections due to axial pressure release. The greatest total deflection (approximately 0.2 mm) is experienced by the longest punch, the LIP; the vertical expansion of the LOP, the shortest one, is less than 0.1 mm. This means that, during axial pressure release, the compact does not remain stationary, as one would expect, but moves slightly upward, pushed by the LIP; gaps are thus generated between the working ends of the LMP and the LOP and the compact, as can be observed in Fig. 26. In this process, the outer flange is partially gripped between the LMP outer wall and the LOP inner wall, due to friction effects. The combination of this restraining action and the upward movement of the LIP places in tension the corner region and this induces, in turn, the formation of the numerically obtained crack.

The above explanation seems to be in accordance with practical experience. Unbalanced punch deflections[29] are one the most common cause of cracking in PM green compacts, especially when dealing with extremely thin parts, as the one under consideration (5.32 mm height). This provides convincing proof of the consistency of the computed results, and proves the ability of the model in reproducing the typology of cracks arising in situations of uncontrolled punch deflections.

5. Conclusion

The primary goal of this work was to explore the possibilities of numerically simulating crack formation during the post-pressing stages in uniaxial die compaction processes. Research effort has been focused on constructing a large strain elasto-plastic constitutive model able to describe, in an unified manner, both the densification of the powder under compressive stress states and the formation of cracks during the post-pressing operations. The introduction of the parabolic plastic potential function has proved successful in reproducing the experimentally observed plastic isochoric behavior in the shear regime, while avoiding the acclaimed numerical shortcomings appearing when jointly using traditional pure isochoric flow rules and implicit integration procedures. Incorporation of a *softening law* – relating cohesion and accumulated plastic shear strain – have enabled us to represent macroscopic cracks as high gradients of inelastic strains concentrated along bands of finite thickness. A novel, thermodynamically consistent calibration procedure has been used to relate material parameters involved in this softening law to fracture energy values obtained experimentally on Distaloy AE specimens. The convergence studies carried out in dealing with the Brazilian test case indicates that the proposed regularization of the softening law, although not very elaborate, have seemed to alleviate the problem of lack of convergence upon refinement of the finite element mesh.

Results presented in Section 4 have largely demonstrated the model's ability to reveal evidence of macroscopic defects and to, at least *qualitatively*, evaluate the influence, in the formation of such cracks, of variations in the input data. The overall impression gained is that the judicious interpretation of cohesion distributions can considerably assist in disclosing and understanding the causes behind experimentally observed cracks. Useful insight can be squeezed from simple qualitative comparisons of cohesion contours obtained from simulation of alternative ejection routes. It should be pointed out that, although the prediction ability of the model has been evaluated only in cases of cracks caused by elastic expansion and/or interaction with the tooling during ejection, there is, in principle, no intrinsic limitation on applying the model

to also describe the formation of other typologies of cracks, such as the so-called *deadwater or shear cracks*, induced by inadequate powder flow around corners during compaction.[30]

Admittedly, there are some flaws in the way the model fits experimental data, in both elastic and plastic regimes, and further research is required to bring computed results into closer agreement with experiments: the characterization of the elastic response, the simplifying assumptions adopted to establish the softening laws, and, perhaps, the numerical technique for modeling the discontinuity associated to a crack, among others, are aspects that should receive further attention. Nevertheless, it should be stressed again that the aim and purpose of the investigation is not to track with fidelity crack growth; any attempt to improve the accuracy and realism of the model must be considered in this light. Too many refinements are not warranted.

Acknowledgments

Appendix A. Fulfilment of the Clausius–Duhem inequality

This appendix is devoted to show that the proposed constitutive model satisfies the requirement of positive dissipation:

$$\mathcal{D} = \boldsymbol{\tau} : \mathbf{d}_p - \overbrace{\left(\frac{\partial \psi_e}{\partial \xi^h} + \frac{\partial \psi_p}{\partial \xi^h}\right) \dot{\xi}^h}^{\dot{\psi}_h} - \overbrace{\frac{\partial \psi_p}{\partial \xi^s} \dot{\xi}^s}^{\dot{\psi}_s} \geqslant 0. \tag{A.1}$$

The associated character of the plastic flow on the elliptical cap and the Von Mises surface, together with the remarks made in Section 2.5 regarding the plastic flow on the Drucker–Prager surface, ensure the positiveness of the rate of plastic work per unit reference volume $\boldsymbol{\tau} : \mathbf{d}_p$. Since the term $\dot{\psi}_s$ accounts for the release of energy associated with softening, that is, $\dot{\psi}_s \leqslant 0$, the worst conceivable circumstances for the satisfaction of inequality (A.1) is when $\dot{\psi}_s = 0$. Therefore, inequality (A.1) can be reduced to:

$$\boldsymbol{\tau} : \mathbf{d}_p \geqslant \frac{\partial \psi_e}{\partial \xi^h} \dot{\xi}^h + \frac{\partial \psi_p}{\partial \xi^h} \dot{\xi}^h, \tag{A.2}$$

i.e., the rate at which energy is *stored* in the powder structure cannot exceed the rate at which plastic work is supplied.

As stated by Eq. (14), the material becomes stiffer as densification progresses. This is reflected also in an increase of internal energy, given by the first term of the right hand side of inequality (A.2):

$$\frac{\partial \psi_e}{\partial \xi^h} \dot{\xi}^h = \frac{1}{2}\left(3\frac{\partial \kappa^e}{\partial \xi^h} \text{tr}^2\ \mathbf{e}_e + 2\frac{\partial \mu^e}{\partial \xi^h}\ dev\ \mathbf{e}_e : dev\ \mathbf{e}_e\right)\dot{\xi}^h. \tag{A.3}$$

Albeit the increase of the bulk and shear modulus, represented by the derivatives $\partial \kappa^e / \partial \xi^h$ and $\partial \mu^e / \partial \xi^h$, is of the same order as the hardening parameter term $\partial s_1 / \partial \xi^h$, they have weighting factors which are quadratic in the elastic strains, a fact that renders the energetic contribution $\partial \psi_e / \partial \xi^h$ negligible in comparison with the other term of $\dot{\psi}_h$. Therefore, attention will be confined to prove that:

$$\mathcal{D} = \boldsymbol{\tau} : \mathbf{d}_p - \frac{\partial \psi_p}{\partial \xi^h} \dot{\xi}^h \geqslant 0. \tag{A.4}$$

The task of verifying (A.4) is normally accomplished by devising a closed-form analytical expression for ψ_p, so that the set of

---

[29] To reduce the detrimental effects of unbalanced punch deflections, upper punches are usually programmed to maintain a certain level of axial pressure, while the motions of the lower punches are accurately controlled so as to compensate the different axial expansions.

[30] The modeling of compaction shear cracks, as opposed to ejection cracks, has been extensively discussed in the P/M modeling literature (see, for instance: Coube and Riedel, 2000; Tahir and Ariffin, 2006; McDonald et al., 2009).

hardening laws $c_h = c_h(\xi^h)$, $c_v = c_v(\xi^h)$ and $s_1 = s_1(\xi^h)$ could be derived by differentiation of ψ_p with respect to ξ^h. In the work by Bier and Hartmann (2006), for instance, this is done by postulating the additive split of the plastic free energy into several parts, each one of them accounting for a different hardening mechanism. Their constitutive model is amenable to such decomposition because they employ a unique function for describing the yield condition and, hence, any transformation of the yield surface in stress space can be easily associated with a combination of simple isotropic (expansion), kinematic (translation) and distortional (change of shape) hardening mechanism. In the problem at hand, however, hardening behavior is not represented by a unique function, but by three evolving surfaces; this fact makes rather difficult to define separately pure expansions, translations and distortions of the yield condition, and, consequently, to derive an analytical form for ψ_p.

In view of these difficulties, it is necessary to retrace the analysis from a more pragmatic perspective, appealing to physical insight and intuition. Note that the primary concern here is not to obtain an expression for ψ_p, but to prove the validity of inequality (A.4). With this observation in mind, consider an alternative constitutive model, characterized solely by an elliptical yield function (Fig. A.28, dashed curve); the flow rule and the equations governing the size of the ellipse are assumed to be the same as those of the original three-yield surfaces model. This model would correspond to a material exhibiting identical mechanical behavior in tension and compression. The existence of a free energy function per unit reference volume, denoted by $\tilde{\psi}$, is also postulated for this idealized *symmetric* material.

Consider now the response predicted by the three-yield surface model and the one corresponding to the elliptical model – henceforth referred to as models *A* and *B*, respectively – under a loading history such that the internal hardening variable ξ^h evolves identically in both cases from ξ^h to $\xi^h + \Delta\xi^h$. Due to interlocking of rough

grains, cold welding of particles and other microscopic events macroscopically correlated with a strain-hardening tendency, the internal energy in the powder material (model *A*) increases by an amount:

$$\Delta\psi = \psi\left(\xi^h + \Delta\xi^h\right) - \psi\left(\xi^h\right); \tag{A.5}$$

in the idealized material (model *B*), this increase is expressed symbolically as

$$\Delta\tilde{\psi} = \tilde{\psi}\left(\xi^h + \Delta\xi^h\right) - \tilde{\psi}\left(\xi^h\right). \tag{A.6}$$

According to the empirical correlations $s_1 = s_1(\xi^h)$ and $c_h = c_h(\xi^h)$, given in Eqs. (19) and (21), respectively, for a typical iron based Distaloy AE powder, an increase of ξ^h from, say 0.8 to 0.9, is accompanied by an increase of the hydrostatic yield stress in compression of approximately 125 MPa, whereas the increase of yield stress encountered on stress reversal is just 10 MPa. This gives a ratio increase of strength in (hydrostatic) compression to increase of strength in (hydrostatic) tension of 125/10 = 12.5. By contrast, the raise of strength predicted by model *B* is the same in compression and tension; it seems thus reasonable to expect also a similar trend concerning the energy stored in the internal structure: in the idealized material (model *B*) the increase of the cohesive forces binding the powder particles is greater than that in the real material (model *A*), and this is manifested by a greater amount of stored internal energy:

$$\Delta\tilde{\psi} > \Delta\psi. \tag{A.7}$$

This line of reasoning can be exploited further. A third constitutive model, henceforth referred to as model *C*, is introduced. The yield condition of this model is exactly the same as in model *B*, but no distortional hardening will be considered; i.e., the eccentric-
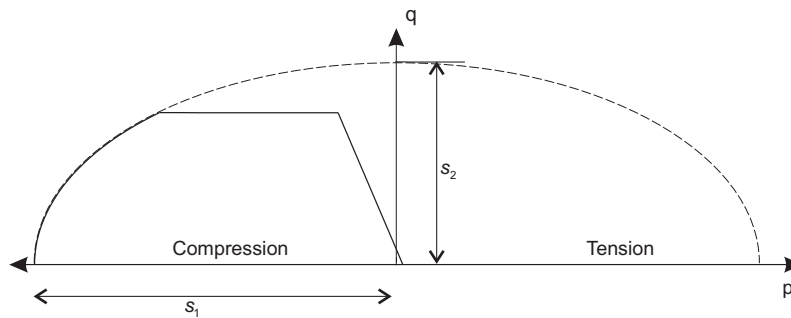

Fig. A.28. Yield condition in the p–q plane for the multisurface model (solid line) and for an *idealized* symmetrical model (dashed line).
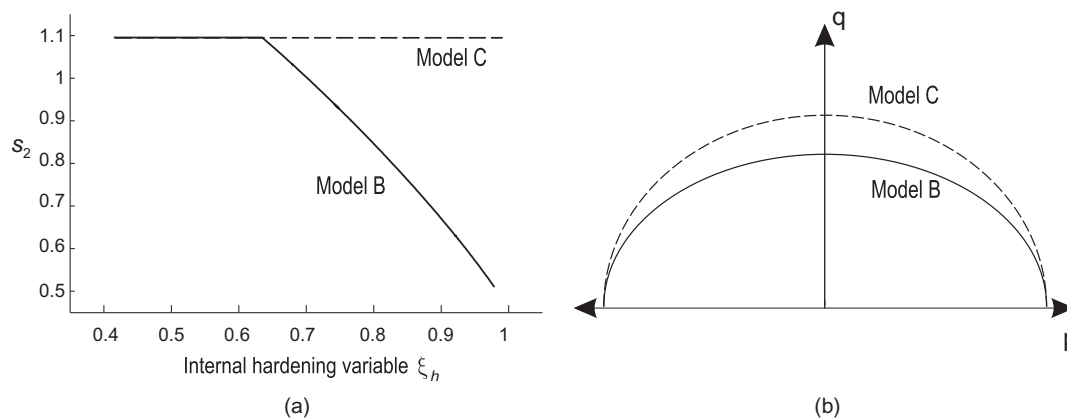

Fig. A.29. (a) Eccentricity of the ellipse for idealized models *B* and *C*. (B) Yield condition for models *B* and *C*.

ity of the ellipse s_2 is regarded as independent of ξ^h, as illustrated in Fig. A.29(a). From this peculiarity, it follows that the yield stress predicted by model C will be equal or greater than that predicted by model B for any loading path (Fig. A.29(b)), inasmuch as $(s_2)_C \geqslant (s_2)_B$. Arguing as above, this implies that:

$$\Delta\hat\psi > \Delta\tilde\psi, \tag{A.8}$$

where $\hat\psi$ denotes the Helmholtz free energy function per unit reference volume associated to model C.

An interesting conclusion can be drawn from inequalities (A.8) and (A.7): for the same increment $\Delta\xi^h$ in the internal hardening variable, the increase in internal energy $\Delta\hat\psi$ corresponding to model C is an *upper bound* of the increase in internal energy $\Delta\psi$ corresponding to the original model. The same conclusion can be couched in terms of dissipation: the dissipation associated to model C is a *lower bound* of the dissipation associated to the original model, $\hat{\mathcal{D}} \leqslant \mathcal{D}$. Therefore, if we show that $\hat{\mathcal{D}} > 0$, where $\hat{\mathcal{D}}$ is the dissipation function for model C, the thermodynamic consistency of the original multisurface model is automatically ensured. The usefulness of our analysis becomes evident at this point: only a hardening mechanism, an expansion characterized by the variable s_1, is active in model C, which can be categorized a simple *isotropic* hardening model. Therefore, the identification of the thermodynamic conjugate of ξ^h in such model is comparatively an easy task, as we show in the following discussion.

Let us write the dissipation function for model C as

$$\hat{\mathcal{D}} = \boldsymbol{\tau} : \mathbf{d}_p - \frac{\partial\hat\psi}{\partial\xi^h}\dot\xi^h. \tag{A.9}$$

In order to avoid a lengthy derivation, we shall recast the definition of the internal hardening variable in a more suitable format. Recall that ξ^h was defined as a function of the length of the trajectory in the plastic strain space through expression:

$$\xi^h(t) = \xi^{h0}\, e^{\int_{t_0}^t \mathrm{tr}\, d_p\, dt}. \tag{A.10}$$

The exponential format of Eq. (A.10) was aimed at defining an internal variable reminiscent of the relative density. For our purpose it is convenient to dispense with this exponential structure and define the internal hardening variable simply as

$$\hat\xi^h(t) = \int_{t_0}^t -\mathrm{tr}\, d_p\, dt \Rightarrow \dot{\hat\xi}^h = -\mathrm{tr}\, d_p = -\frac{\dot\xi^h}{\xi^h}. \tag{A.11}$$

Note that the physical meaning of the internal hardening variable is not altered by this transformation. Eq. (A.9) in terms of $\hat\xi^h$ becomes:

$$\hat{\mathcal{D}} = \boldsymbol{\tau} : d_p - \frac{\partial\hat\psi}{\partial\xi^h}\dot\xi^h = \boldsymbol{\tau} : d_p - \frac{\partial\hat\psi}{\partial\hat\xi^h}\dot{\hat\xi}^h. \tag{A.12}$$

It only remains to choose the thermodynamic conjugate of $\hat\xi^h$. Taking into account that $\mathrm{tr}\mathbf{d}_p$, and hence $\dot{\hat\xi}^h$, is directly related with inelastic volumetric changes, a natural candidate for the conjugate of $\hat\xi^h$ is the hydrostatic yield stress in compression, the state variable s_1:

$$\frac{\partial\hat\psi}{\partial\hat\xi^h} = s_1(\hat\xi^h). \tag{A.13}$$

To complete the analysis, Eqs. (A.13) and (A.11) are substituted in Eq. (A.12), and by rearranging terms, we obtain:

$$\hat{\mathcal{D}} = \boldsymbol{\tau} : d_p + s_1 \mathrm{tr}\, d_p = (p + s_1)\mathrm{tr}\, d_p + dev\, \boldsymbol{\tau} : dev\, d_p. \tag{A.14}$$

By using the flow rule in Eq. (A.13), we get:

$$\hat{\mathcal{D}} = 2\dot\lambda^e\, (s_2^2\, p\, (p + s_1) + q^2). \tag{A.15}$$

Finally, to study the sign of Eq. (A.15), the norm of the deviatoric stress q is expressed as a function of p and s_1, yielding:

$$\hat{\mathcal{D}} = 2\dot\lambda^e (s_2^2 p(p + s_1) + s_2^2(s_1^2 - p^2)) = 2\dot\lambda^e s_2^2 s_1(p + s_1). \tag{A.16}$$

Since $\dot\lambda^e \geqslant 0$ and $|p| \leqslant s_1$, it follows from Eq. (A.16) that $\hat{\mathcal{D}} \geqslant 0$. Thus, the requirement of positive dissipation is satisfied by model C and, as we stated above, this provides the assurance that our multisurface constitutive model is consistent with the second law of the thermodynamics.

References

Agelet de Saracibar, C., Chiumenti, M., Valverde, Q., Cervera, M., 2006. On the orthogonal subgrid scale pressure stabilization of finite deformation j2 plasticity. Computer Methods in Applied Mechanics and Engineering 195, 1224–1251.

Belytschko, T., Liu, W.K., Moran, B., 2001. Nonlinear Finite Elements for Continua and Structures. John Wiley and Sons Ltd., New York.

Belytschko, T., Mish, K., 2001. Computability in non-linear solid mechanics. International Journal for Numerical Methods in Engineering 52, 3–21.

Bicánic, N., Pearce, C.J., 1998. Computational aspects of a softening plasticity model for plain concrete. Mechanics of Cohesive-Frictional Materials 1 (1), 75–94.

Bier, W., Hartmann, S., 2006. A finite strain constitutive model for metal powder compaction using a unique and convex single surface yield function. European Journal of Mechanics 25, 1009–1030.

Brekelmans, W.A.M., Janssen, J.D., de Ven, A.A.F.V., 1991. An eulerian approach for die compaction processes. International Journal for Numerical Methods in Engineering 31, 509–524.

Brewin, P., Coube, O., Doremus, P., Tweed, J., 2007. Modelling of Powder Die Compaction. Springer-Verlag.

Brewin, P., Federzoni, L., 2006. Dienet: conclusions and achievements. Powder Metallurgy 49, 8–10.

Broek, D., 1988. The Practical Use of Fracture Mechanics. Kluwer Academic Publishers.

Brown, S.B., Weber, G.G.A., 1988. A constitutive model for the compaction of metal powders. Modern Developments in Powder Metallurgy 18, 465–476.

Cante, J.C., 1995. Simulación numérica de procesos de compactación de pulvimateriales. Aplicación de técnicas de cálculo paralelo, PhD Thesis, Technical University of Cataluña, Barcelona (in Spanish).

Cante, J.C., Oliver, J., González, C., Calero, J.A., Benítez, F., 2005. On numerical simulation of powder compaction processes: powder transfer modelling and characterisation. Powder Metallurgy 48, 85–92.

Cervera, M., Chiumenti, M., Agelet de Saracibar, C., 2004. Softening, localization and stabilization: capture of discontinuous solutions in j2 plasticity. International Journal for Numerical and Analytical Methods in Geomechanics 28, 373–393.

Chtourou, H., Gakwaya, A., Guillot, M., 2002a. Modeling of the metal powder compaction process using the cap model. Part II: numerical implementation and practical applications. International Journal of Solids and Structures 39, 1077–1096.

Chtourou, H., Guillota, M., Gakwaya, A., 2002b. Modeling of the metal powder compaction process using the cap model. Part I: experimental material characterization and validation. International Journal of Solids and Structures 39, 1059–1075.

Cocks, A.C.F., Sinka, I.C., 2006. Constitutive modelling of powder compaction I. Theoretical concepts. Mechanics of Materials 39, 392–403.

Coube, O., 1998. Modelling and numerical simulation of powder die compaction with consideration of cracking, PhD Thesis, University Pierre et Marie Curie, Paris VI, Paris.

Coube, O., Riedel, H., 2000. Numerical simulation of metal powder die compaction with special consideration of cracking. Powder Metallurgy 43, 123–131.

Crisfield, M.A., 1991. Non-linear finite element analysis of solids and structures. Essentials, vol. 1. John Wiley and Sons Ltd., Chichester.

Cunningham, J.C., 2005. Experimental studies and modeling of the roller compaction of pharmaceutical powders, PhD Thesis, Drexel University.

de Borst, R., 2001. Some recent issues in computational failure mechanics. International Journal for Numerical Methods in Engineering 52, 63–95.

Doremus, P., Toussaint, F., Alvain, O., 2001. Simple tests and standard procedure for the characterization of green compacted powder. In: Zavaliangos, A., Lapter, A. (Eds.), Recent developments in Computer Modeling of Powder Metallurgy Processes. IOS press, pp. 277–285.

Duxbury, P., Li, X., 1996. Development of elasto-plastic material models in a natural coordinate system. Computer Methods in Applied Mechanics and Engineering 135, 283–306.

Erhart, T., Wall, W.A., Ramm, E., 2005. A robust computational approach for dry powders under quasi-static and transient impact loadings. Computer Methods in Applied Mechanics and Engineering 194, 4115–4134.

Etse, G., Willam, K.J., 1994. A fracture-energy based constitutive formulation for inelastic behavior of plain concrete. Journal of Engineering Mechanics 120, 1983–2011.

Federzoni, L., Riedel, H., Coube, O., Oldenburg, M., Gethin, D., Mosbah, P., Virta, J., Martikainen, H., Frachon, A., Doremus, P., et al., 1999. State of the art review: comparison of computer models representing powder compaction process. Powder Metallurgy 42 (4), 301–311.

Fleck, N.A., 1995. On the cold compaction of powders. Journal of the Mechanics and Physics of Solids 43, 1409–1431.

Grassl, P., Jiràsek, M., 2006. Damage-plastic model for concrete failure. International Journal of Solids and Structures 43, 7166–7196.

Hartmann, S., Oliver, J., Cante, J.C., Weyler, R., Hernández, J.A., 2009. A contact domain method for large deformation frictional contact problems. Part 2: numerical aspects. Computer Methods in Applied Mechanics and Engineering 198, 2607–2631.

Hartmann, S., Weyler, R., Oliver, J., Cante, J.C., Hernández, J.A., 2010. A 3D frictionless contact domain method for large deformation problems. Computer Modeling in Engineering & Sciences 55, 211–270.

Hearn, E.J., 2000. Mechanics of Materials I. Butterworth-Heinemann, Oxford.

Hernández, J., 2009. Numerical modeling of crack formation in powder compaction based manufacturing problems, PhD Thesis, Technical University of Catalonia, Barcelona.

Jonsén, P., Häggblad, H., 2007. Fracture energy based constitutive models for tensile fracture of metal powder compacts. International Journal of Solids and Structures 44, 6398–6411.

Jonsén, P., Häggblad, H.-A., Sommer, K., 2007. Tensile strength and fracture energy of pressed metal powder by diametral compression test. Powder Technology 176, 148–155.

Khan, A.S., Huang, S., 1995. Continuum Theory of Plasticity. Wiley, New York.

Kuhl, E., Ramm, E., Willam, K., 2000. Failure analysis of elasto-plastic material models on diferent levels of observation. International Journal of Solids and Structures 37, 7259–7280.

Lewis, R.W., Khoei, A.R., 2001. Numerical analysis of strain localization in metal powder-forming processes. Internation Journal for Numerical Methods in Engineering 52, 489–501.

Lubliner, J., 1990. Plasticity Theory. McMillan, New York.

Mähler, L., Runesson, K., 2003. Constitutive modeling of cold compaction and sintering of hardmetal. Journal of Engineering Materials and Technology 125, 191–199.

McDonald, S., Motazedian, F., Cocks, A., Withers, P., 2009. Shear cracking in an Al powder compact studied by X-ray microtomography. Materials Science and Engineering: A 508 (1–2), 64–70.

Mosbah, P., 1995. Etude expérimentale et modélisation du comportement de poudres métalliques au cours du compactage en matrice fermée, PhD Thesis, Université Joseph Fourier-Grenoble I (in French).

Mosler, J., Meschke, G., 2004. Embedded crack vs.smeared crack models: a comparison of elementwise discontinuous crack path approaches with emphasis on mesh bias. Computer Methods in Applied Mechanics and Engineering 193, 3351–3375.

Oliver, J., 1989. A consistent characteristic length for smeared cracking models. International Journal for Numerical Methods in Engineering 28, 461–474.

Oliver, J., 1996. Modelling strong discontinuities in solid mechanics via strain softening constitutive equations. Internation Journal for Numerical Methods in Engineering 39, 3575–3600.

Oliver, J., 2000. On the discrete constitutive models induced by strong discontinuity kinematics and continuum constitutive equations. International Journal of Solids and Structures 37, 7207–7229.

Oliver, J., Cante, J.C., Weyler, R., González, C., Hernández, J.A., 2007. Particle Finite Element Methods in Solid Mechanics. Computational Plasticity. Springer.

Oliver, J., Hartmann, S., Cante, J.C., Weyler, R., Hernández, J.A., 2009. A contact domain method for large deformation frictional contact problems. Part 1: theoretical basis. Computer Methods in Applied Mechanics and Engineering 198, 2591–2606.

Oliver, J., Huespe, A.E., Blanco, S., Linero, D.L., 2006. Stability and robustness issues in numerical modeling of material failure with the strong discontinuity approach. Computer Methods in Applied Mechanics and Engineering 195, 7093–7114.

Oliver, J., Huespe, A.E., Cante, J.C., 2008. An implicit/explicit integration scheme to increase computability of non-linear material and contact/friction problems. Computer Methods in Applied Mechanics and Engineering 197, 1865–1889.

Oliver, J., Oller, S., Cante, J.C., 1996. A plasticity model for simulation of industrial powder compaction processes. Journal of Solids and Structures 33, 3161–3178.

Oller, S., 1998. Un modelo de daño continuo para materiales friccionales, PhD Thesis, Technical University of Cataluña, Barcelona (in Spanish).

Pavier, E., 1998. Caracterisation du comportement d'une poudre de fer pour le procede de compression en matrice, PhD Thesis, L'Institut National Polytechnique de Grenoble.

Pavier, E., Dorémus, P., 1996. Mechanical behavior of a lubricated iron powder. In: Powder Metallurgy PM96. Advances in Powder Metallurgy and Particulate Materials, vol. 6, pp. 27–40.

PM Modnet Computer Modelling Group, 1999. Comparison of computer models representing powder compaction process. Powder Metallurgy 42, 301–311.

Regueiro, R.A., Borja, R.I., 1999. A finite element model of localized deformation in frictional materials taking a strong discontinuity approach. Finite Elements in Analysis and Design 33, 283–315.

Riera, M.D., 1999. Comportamiento elastoplástico de compactos pulvimetalúrgicos, PhD Thesis, Technical University of Cataluña, Barcelona.

Rossi, R., Alves, M.K., Qureshi, H.A.A., 2007. A model for the simulation of powder compaction processes. Journal of Materials Processing Technology 182, 286–296.

Simo, J.C., 1999. Topics on the numerical analysis and simulation of plasticity. In: Ciarlet, P.G., Lions, J.L. (Eds.), Handbook of Numerical Analysis, vol. III. Elsevier Science Publisher, Amsterdam.

Simo, J.C., Hughes, T.J.R., 1998. Computational Inelasticity. Springer, New York.

Sinka, I.C., Cocks, A.C.F., 2007. Constitutive modelling of powder compaction II. Evaluation of material data. Mechanics of Materials 39, 404–416.

Storåkers, B., Fleck, N.A., McMeeking, R.M., 1999. The viscoplastic compaction of composite powders. Journal of Mechanics and Physics of Solids 47, 785–815.

Tahir, S.M., Ariffin, A.K., 2006. Fracture in metal powder compaction. International Journal of Solids and Structures 43, 1528–1542.

Timoshenko, S.P., Goodier, J.N., 1970. Theory of Elasticity. McGraw-Hill.

Tszeng, T.C., Wu, W.T., 1996. A study of the coefficients in yield functions modeling metal powder deformation. Acta Metallurgica 44, 3543–3552.

Vrech, S.M., Etse, G., 2006. Geometrical localization analysis of gradient-dependent parabolic drucker-prager elastoplasticity. International Journal of Plasticity 22, 943–964.

Wanga, Q.Z., Jiaa, X.M., Koub, S.Q., Zhangb, Z.X., Lindqvistb, P.A., 2003. The flattened brazilian disc specimen used for testing elastic modulus, tensile strength and fracture toughness of brittle rocks: analytical and numerical results. International Journal of Rock Mechanics and Mining Sciences 41, 245–253.

Weyler, R., 2000. Simulación numérica de procesos de compactación y extrusión de materiales pulverulentos, PhD Thesis, Technical University of Cataluña, Barcelona (in Spanish).

Zenger, D., Cai, H., 1997. Handbook of the Common Cracks in Green P/M Compacts. Metal Powder Industry Federation, Worcester.